Journal of Computational Physics 228 (2009) 1830–1861

Contents lists available at ScienceDirect

Journal of Computational Physics

journal homepage: www.elsevier.com/locate/jcp

A family of dynamic finite difference schemes for large-eddy simulation

Dieter Fauconnier *, Chris De Langhe, Erik Dick

Department of Flow, Heat and Combustion Mechanics, Ghent University, St. Pietersnieuwstraat 41, B-9000 Ghent, Belgium

ARTICLE INFO

Article history:
Received 19 May 2008
Received in revised form 28 October 2008
Accepted 12 November 2008
Available online 27 November 2008

Keywords:
Dynamic finite difference schemes
Dispersion-relation preserving schemes
Large-eddy simulation
Dynamic procedure
Richardson extrapolation

ABSTRACT

A family of *dynamic* low-dispersive finite difference schemes for large-eddy simulation is developed. The dynamic schemes are constructed by combining Taylor series expansions on two different grid resolutions. The schemes are optimized dynamically during the simulation according to the flow physics and dispersion errors are minimized through the real-time adaption of the dynamic coefficient. In case of DNS-resolution, the dynamic schemes reduce to the standard Taylor-based finite difference schemes with formal asymptotic order of accuracy. When going to LES-resolution, the schemes seamlessly adapt to dispersion-relation preserving schemes. The schemes are tested for large-eddy simulation of Burgers' equation and numerical errors are investigated as well as their interaction with the subgrid model. Very good results are obtained.

1. Introduction

In the past decades, the necessity for numerical quality in direct numerical simulations (DNS) and large-eddy simulations (LES) of turbulent flows, has been recognized by many researchers, e.g. [1–3]. In a very well resolved direct numerical simulation, the smallest resolved scales are located far into the dissipation range. Since these scales have only a very small energy-content in comparison with the largest resolved scales in the flow, they are often considered to have a negligible influence on the mean flow statistics. In a large-eddy simulation, however, where only the most important large scale structures are resolved, the smallest resolved scales are part of the inertial subrange such that they contain relatively more energy than those in the dissipation range. Hence, the smallest resolved scales in large-eddy simulation are not negligible and have a significant influence on the evolution of the LES-flow. The accuracy with which these small scales are described is therefore expected to be important. Moreover, some advanced subgrid modeling techniques such as the dynamic procedure or multiscale modeling strongly rely on the smallest resolved scales in LES. Hence, accurate resolution of the small scales should result in correct application of these subgrid models. Good numerical quality for an affordable LES is thus vital for accurate flow prediction as it directly influences resolved physics as well as subgrid modeling.

Aside from aliasing errors, which should be prevented by eliminating scales beyond $\kappa_c = 2/3\kappa_{max}$ [4], discretization errors are mainly responsible for the loss of numerical accuracy. In order to reduce the computational costs, it is highly desirable in LES to maximize the ratio between the physical resolution and the grid resolution κ_c/κ_{max}. Standard second-order central schemes may not be sufficient for accurate LES, since numerical errors can become dominant for large κ_c/κ_{max}. Ghosal [1] and Chow and Moin [3] recommend a filter-to-grid cutoff-ratio $\kappa_c/\kappa_{max} \leqslant 1/4$ when using a second-order central scheme, to ensure that the magnitudes of the discretization errors remain smaller than the magnitude of the modeled force of the subgrid scales. However, in contrast to Ghosal [1] and Chow and Moin [3], Park and Mahesh [5] found in the Eddy-Damped Quasi-Normal Markovian LES or EDQNM-LES of isotropic turbulence at low Reynolds number, that for a second-order

* Corresponding author. Tel.: +32 9 264 95 21; fax: +32 9 264 35 86.
E-mail address: dieter.fauconnier@ugent.be (D. Fauconnier).

0021-9991/$ - see front matter © 2008 Elsevier Inc. All rights reserved.
doi:10.1016/j.jcp.2008.11.014

scheme, the subgrid force remains dominant. Indeed, for low Reynolds numbers, the finite difference approximation of the subgrid force is relatively more important than for high Reynolds numbers [6], leading to somewhat different results and conclusions. Nevertheless, for high Reynolds numbers, the numerical error of the nonlinear term is dominant and can be larger than the subgrid force as shown by Berland et al. [6] using EDQNM theory. Moreover, since accurate resolution of the smallest scales (characterized by κ_c) increases the required number of nodes with a factor $(2\kappa_{max}/3\kappa_c)^3$ than theoretically necessary, such small values of κ_c/κ_{max} are prohibitively expensive for most 3D LES computations. Higher-order discretizations are often applied to allow for larger filter-to-grid cutoff-ratios. However, in order to obtain acceptable dispersion errors up to $\kappa_c = 2/3\kappa_{max}$, which is the maximum resolution on the computational grid, at least the standard 10th-order central scheme or a sixth-order compact Padé scheme are required, which again inevitably leads to increased complexity and/or computational costs.

It is common practice in computational fluid dynamics to use (high-order) central schemes based on a truncated Taylor series, leading to a certain formal asymptotic order of accuracy for the largest scales. Although this may be sufficient for fully resolved direct numerical simulations, it is not necessarily the optimal strategy for large-eddy simulation. Preserving the global dispersion relation for the full range of scales up to $\kappa_c = 2/3\kappa_{max}$ instead of focusing on asymptotic order of convergence, could be much more advantageous in large-eddy simulations. In other words, it may be desirable for LES to have optimized finite difference approximations of the derivatives with similar Fourier characteristics as the analytical derivatives. This point of view was introduced by Tam and Webb [7] in the field of computational aeroacoustics, where accurate simulation of propagating waves require highly non-dispersive and non-dissipative finite difference schemes. Kim and Lee [8], Hixon [9], Ashcroft and Zhang [10], Bogey and Bailly [11] and Berland et al. [6] performed further investigations on this topic. These low-dispersive prefactored finite difference schemes are constructed by static minimization of the dispersion errors in Fourier space in the range $0 \leqslant \kappa_c/\kappa_{max} \leqslant 0.9$, assuming a uniform spectrum distribution.

In the present work, we develop a family of *dynamic* low-dispersive finite difference schemes for large-eddy simulation. The schemes, inspired by the work of Winckelmans et al. [12,13], Debliquy et al. [14] and Knaepen et al. [15], are constructed by combining Taylor expansions on two different grid resolutions, similar to Richardson Extrapolation. A first attempt of this technique has proven successful for obtaining higher accuracy in laminar flows in Fauconnier et al. [16,17]. Here, we try to refine the technique for large-eddy simulation, and show the agreements with the work of Tam and Webb [7] and Kim and Lee [8]. However, in contrast to their work, the constructed schemes are optimized dynamically during the simulation according to the instantaneous properties of the flow and dispersion errors are minimized through the real-time adaption of a dynamic coefficient. In case of DNS-resolution, i.e. for sufficiently smooth and regular physics on the grid, the dynamic schemes reduce to the standard Taylor-based finite difference schemes with formal asymptotic order of accuracy. When going to LES-resolution, the schemes seamlessly adapt to optimized schemes. This could be particularly interesting for transient developing flows, or in case of grid refinement studies with fixed filter width.

The outline of this paper is as follows: after a short description of the mathematical formalism of discretization, the dynamic finite difference approximations are constructed by combining Taylor series expansions on two different grid resolutions. The accuracy of the constructed schemes is analyzed in Fourier space using modified wavenumbers. Since one variant of these schemes is nonlinear, a multiple-wave Fourier analysis of the transfer function is done [16]. The relation of the dynamic schemes with the dispersion-relation preserving (DRP) scheme of Tam and Webb [7] and the dispersion-relation preserving compact Padé scheme of Kim and Lee [8] is then demonstrated. The remaining parameter in the dynamic schemes is then optimized, using a model for the expected energy spectrum. The effect of the specific choice of the spectrum on this parameter is discussed. Before presenting the results obtained from the large-eddy simulation of the one-dimensional viscous Burgers' equation, the numerical setup and the definitions for error evaluation of the finite difference schemes are briefly explained. The current LES-approach on the Burgers' equation is different from previous studies of dispersion-relation preserving schemes in which either linear wave propagation problems [8,10,18], or simulations of inviscid Burgers' or Euler equations without dealiasing nor *subgrid* dissipation [9] were studied. In this work, dealiasing is implemented as proposed by Orszag [4] in order to exclude aliasing errors from the solution. An error decomposition is defined as an attempt to separate the finite difference errors from modeling errors [19,20]. Moreover, the influence on the dynamic Smagorinsky-like model is investigated. Finally the conclusions are presented. To the authors' knowledge only Berland et al. [6] have performed an error quantification of prefactored dispersion-relation preserving schemes using EDQNM-closed large-eddy simulation of isotropic turbulence. The present work might be a first attempt for a systematical study on the topic of general dispersion-relation preserving schemes for LES in physical space.

2. Mathematical formalism

Assume a vector field $\vec{u}(\vec{x},t)$ defined in continuum space $\mathbb{R}^q$, $q \in \{1,2,3\}$. To avoid an overload in notation, we restrict ourselves in this work to one spatial dimension $q = 1$, without loss of generality and we do not write explicitly the dimension in time, such that $u(x,t) = u(x) \in \mathbb{R}$. Consider now the definition of the continuum nth-order spatial derivative of this field,

$$\frac{\partial^n u}{\partial x^n} = \lim_{\delta \to \epsilon} \frac{\delta^n u}{(\delta x)^n}, \tag{1}$$

with $\epsilon \to 0$ an infinitesimal interval. Since this definition cannot be satisfied in discrete space, where inevitably $\epsilon > 0$, the derivative can only have a discrete approximation constructed from a Taylor series expansion to a certain order of accuracy

k. Using the notation $\bar{u}$ for the discrete field and δ for the discrete difference operator, Taylor series expansion for the derivative reads

$$\overline{\frac{\partial^n u}{\partial x^n}} = \frac{\delta^n \bar{u}}{\delta x^n} + c_{k,n} \Delta x^k \overline{\frac{\partial^{n+k} u}{\partial x^{n+k}}} + \mathcal{O}(\Delta x^{k+2}), \tag{2}$$

in which the finite difference approximation in a node $x = x_j$ is

$$\frac{\delta^n \bar{u}}{\delta x^n} = \frac{1}{\Delta x^n} \sum_{m=j-r}^{j+r} \beta_m \bar{u}(x_j), \tag{3}$$

r being the number of neighboring grid points used in the approximation and β_m a set of weighting coefficients. Since DNS and LES are very sensitive to numerical dissipation, which can excessively damp small scales, only central schemes will be considered, having a symmetric set of coefficients β_m. Although these central schemes are non-dissipative, they can induce dispersion errors, affecting the phase speed of the separate wave components and redistributing energy. For regular fields, which are sufficiently smooth on the computational grid, the Taylor series converges rapidly due to small contributions of the higher derivatives. Hence, the dispersion errors remain low. However, in case of highly fluctuating fields with marginal resolution on the grid, the contributions of the higher derivatives in the truncation terms of the Taylor series become much more important, slowing down the convergence of the Taylor series and thus leading to significant dispersion errors. Standard Taylor-based asymptotic finite difference approximations assume smooth fields and fast convergence of the Taylor series. However, in case of irregular LES-fields, where the Taylor series converges more slowly, it would be much more advantageous to minimize contributions of all terms in the Taylor series to obtain good overall performance. In the next paragraph, we construct highly accurate central schemes with minimized dispersion errors, by comparing Taylor series on two different grid resolutions. We therefore extend the previous mathematical formulation to multi-resolution formulation.

We define two grid resolutions with grid spacings Δ and 2Δ. The exact Taylor series expansions for the nth-order derivative, $n = 0, 1, 2, \ldots$, for a kth-order central discretization scheme ($k = 2, 4, 6, \ldots$) on the two grid resolutions are given by

$$\overline{\frac{\partial^n u}{\partial x^n}}(x) = \left.\frac{\delta^n \bar{u}}{\delta x^n}\right|^{\Delta} + c_{k,n} \Delta^k \overline{\frac{\partial^{k+n} u}{\partial x^{k+n}}} + \mathcal{O}(\Delta^{k+2}), \tag{4}$$

$$\overline{\frac{\partial^n u}{\partial x^n}}(x) = \left.\frac{\delta^n \bar{u}}{\delta x^n}\right|^{2\Delta} + c_{k,n} (2\Delta)^k \overline{\frac{\partial^{k+n} u}{\partial x^{k+n}}} + \mathcal{O}(\Delta^{k+2}), \tag{5}$$

in which the coefficient $c_{k,n}$ is known a priori from Taylor series expansion. In the following, we denote this theoretical Taylor value as $c^*_{k,n}$. Two common techniques exist now to obtain higher-order approximations. One can either find a finite difference approximation for the leading order truncation terms, or eliminate the coefficient $c_{k,n}$ by combining expressions (4) and (5), truncated to order $\mathcal{O}(\Delta^{k+2})$. The latter technique, known as Richardson extrapolation, has no clear advantage over the first one, since both lead to a finite difference approximation of formal order of accuracy $\mathcal{O}(\Delta^{k+2})$. However, we show in this work that the combination of both techniques can lead to a non-trivial self-adaptive dynamic scheme with basic order of accuracy $\mathcal{O}(\Delta^k)$, but with better spectral characteristics.

3. Construction of the dynamic finite difference schemes

Suppose the leading order truncation terms in Taylor series (4) and (5) are discretized on both grid resolutions with a minimal order $\mathcal{O}(\Delta^2)$. Then it would be possible to obtain a value of $c_{k,n}$ by combining both expressions. The new $c_{k,n}$ will not necessarily have the same value as the one obtained from the Taylor series, as it is a function of $u(x)$ and its derivatives. Moreover, we expect the value of $c_{k,n}$ to be optimized with respect to $u(x)$, such that deficiencies of the finite difference approximation, e.g. dispersion errors are minimized.

We proceed by writing the truncated Taylor series with the discretized leading order truncation term and we introduce a blending factor f in the second equation

$$\overline{\frac{\partial^n u}{\partial x^n}}(x) = \left.\frac{\delta^n \bar{u}}{\delta x^n}\right|^{\Delta} + c_{k,n} \Delta^k \left.\frac{\delta^{k+n} \bar{u}}{\delta x^{k+n}}\right|^{\Delta} + \mathcal{O}(\Delta^k), \tag{6}$$

$$\overline{\frac{\partial^n u}{\partial x^n}}(x) = \left.\frac{\delta^n \bar{u}}{\delta x^n}\right|^{2\Delta} + c_{k,n} (2\Delta)^k \left\{ f \left.\frac{\delta^{k+n} \bar{u}}{\delta x^{k+n}}\right|^{2\Delta} + (1-f) \left.\frac{\delta^{k+n} \bar{u}}{\delta x^{k+n}}\right|^{\Delta} \right\} + \mathcal{O}((2\Delta)^k). \tag{7}$$

Remark that, unless $c_{k,n}$ has the exact Taylor value, the order of accuracy in both expressions remains $\mathcal{O}(\Delta^k)$. The difference between the fine grid and coarse grid discretization is obtained by subtracting (7) from (6) giving

$$\mathcal{E} = \mathcal{L} + c_{k,n} \mathcal{M} = \mathcal{O}((2\Delta)^k) - \mathcal{O}(\Delta^k), \tag{8}$$

in which the *Leonard terms* $\mathcal{L}$ and the *Model terms* $\mathcal{M}$ read

$$\mathcal{L} = \left|\frac{\delta^n \bar{u}}{\delta x^n}\right|^{\Delta} - \left|\frac{\delta^n \bar{u}}{\delta x^n}\right|^{2\Delta}, \tag{9}$$

$$\mathcal{M} = (1-2^k)\Delta^k \left|\frac{\delta^{k+n}\bar{u}}{\delta x^{k+n}}\right|^{\Delta} - 2^k \Delta^k f \left(\left|\frac{\delta^{k+n}\bar{u}}{\delta x^{k+n}}\right|^{2\Delta} - \left|\frac{\delta^{k+n}\bar{u}}{\delta x^{k+n}}\right|^{\Delta}\right). \tag{10}$$

The magnitude of the difference (8), which is a function of the parameter $c_{k,n}$, provides an indication about the accuracy with which the finite difference scheme on the fine grid resolution approximates the analytical derivative. If the difference is small, the resolution is sufficiently fine and ensures an accurate finite difference approximation on the fine grid. In contrast, a large difference $\mathcal{E}$ indicates that the resolution is not fine enough to guarantee a good accuracy of the finite difference approximation on the fine grid. However, an optimal coefficient $c_{k,n}$ can be found such that the difference $\mathcal{E}$ is minimal. Then, the finite difference approximation on the fine grid must have an optimal accuracy (low dispersion error), which differs only minimally with the accuracy of the coarse grid approximation. To explain the purpose of the blending factor $f \in [0,1]$ we illustrate the cases $f = 0$ and $f \neq 0$.

3.1. Asymptotic high-order schemes for $f = 0$

If the blending factor $f = 0$, then the coefficient $c_{k,n}$ can be obtained from expression (8) by imposing the difference $\mathcal{E} = 0$, leading to

$$\left|\frac{\delta^n \bar{u}}{\delta x^n}\right|^{\Delta} - \left|\frac{\delta^n \bar{u}}{\delta x^n}\right|^{2\Delta} = c_{k,n}(2^k - 1)\Delta^k \left|\frac{\delta^{k+n}\bar{u}}{\delta x^{k+n}}\right|^{\Delta}. \tag{11}$$

Although the left-hand-side discretization does not necessarily lead to a finite difference approximation of $\delta^{k+n}\bar{u}/\delta x^{k+n}|^{\Delta}$ with minimal stencil width, we consider in this work $\delta^{k+n}\bar{u}/\delta x^{k+n}|^{\Delta}$ be discretized with minimal stencil width. Substitution of (11) into (6), eliminating $c_{k,n}$ leads to the finite difference approximation of order $\mathcal{O}(\Delta^{k+2})$.

$$\frac{\overline{\partial^n u}}{\partial x^n}(x) = \frac{2^k \left|\frac{\delta^n \bar{u}}{\delta x^n}\right|^{\Delta} - \left|\frac{\delta^n \bar{u}}{\delta x^n}\right|^{2\Delta}}{2^k - 1} + \mathcal{O}(\Delta^{k+2}), \tag{12}$$

which is Richardson's Extrapolation formula. Expression (12) is thus again an approximation with formal asymptotic order of accuracy $\mathcal{O}(\Delta^{k+2})$. Since the aim is to construct optimized finite difference schemes with good Fourier characteristics, abandoning the concept of formal asymptotic order of accuracy, we investigate the case where f is different from zero.

3.2. Optimized schemes for $f \neq 0$

For the case $f \neq 0$, we proceed in a somewhat different manner than for $f = 0$. Imposing $\mathcal{E} = 0$ and eliminating $c_{k,n}$ straightforwardly from expression (8), would lead to a substitution of $c_{k,n}$ with a nonlinear expression. The resulting field for $c_{k,n}$ would be pointwise varying in space, in contrast to the constant value obtained from the Taylor series. Here, we follow a more general approach instead by extracting $c_{k,n}$ from a least squares optimization, in which the least squares averaging domain is an additional degree of freedom. This allows us to regulate the smoothness of the obtained coefficient. We proceed by subtracting (7) from (6). First, expressions (9) and (10) can be simplified by writing them on a single grid resolution using relation (11)

$$\mathcal{L} = c^*_{k,n}(2^k - 1)\Delta^k \left|\frac{\delta^{k+n}\bar{u}}{\delta x^{k+n}}\right|^{\Delta}, \tag{13}$$

$$\mathcal{M} = (1-2^k)\Delta^k \left|\frac{\delta^{k+n}\bar{u}}{\delta x^{k+n}}\right|^{\Delta} - 2^k \Delta^k f \left(c^{**}_{k,n}(1-2^2)\Delta^2 \left|\frac{\delta^{k+n+2}\bar{u}}{\delta x^{k+n+2}}\right|^{\Delta}\right), \tag{14}$$

with $c^*_{k,n}$ and $c^{**}_{k,n}$ constant coefficients known from Taylor series expansion. Note that $c^*_{k,n}$ and $c^{**}_{k,n}$ differ for different derivatives. The optimized coefficient can be extracted by least squares minimization of the difference $\mathcal{E}$, i.e.

$$\frac{\partial}{\partial c_{k,n}}\langle \mathcal{E}^2 \rangle = 0, \tag{15}$$

where $\langle \cdot \rangle$ denotes an averaging operator (to be defined later), resulting finally in the dynamic coefficient

$$c^{dyn}_{k,n} = -\frac{\langle \mathcal{L}\mathcal{M} \rangle}{\langle \mathcal{M}\mathcal{M} \rangle}. \tag{16}$$

Once $c^{dyn}_{k,n}$ is calculated, its value can be used in the expression

$$\overline{\frac{\partial^n u}{\partial x^n}}(x) = \frac{\delta^n \bar{u}}{\delta x^n}\bigg|^{\Delta} + c_{k,n}^{dyn}\Delta^k \frac{\delta^{k+n}\bar{u}}{\delta x^{k+n}}\bigg|^{\Delta} + \mathcal{O}(\Delta^k). \tag{17}$$

The resulting dynamic scheme has a formal order of accuracy $\mathcal{O}(\Delta^k)$ unless $c_{k,n}^{dyn}$ equals the Taylor value which then leads to formal order of accuracy $\mathcal{O}(\Delta^{k+2})$. Although the order of accuracy is not necessarily increased by this dynamic procedure, the scheme can have better Fourier characteristics. This will be shown in next paragraph.

In this work, only two averaging operations are considered, i.e. a global uniform averaging over the entire domain, and a local averaging over half the grid spacing $\Delta/2$. Clearly it is possible to perform local averaging over multiple grid spacings, but this case will not be considered in the present work. Applying the global uniform averaging operator to expression (16) results into the following spatially constant coefficient

$$c_{k,n}^{dyn} = c_{k,n}^{*}\frac{\left\langle \left[\frac{\delta^{k+n}\bar{u}^2}{\delta x^{k+n}} - \frac{2^k(1-2^2)}{1-2^k} f c_{k,n}^{**}\Delta^2 \frac{\delta^{k+n+2}\bar{u}}{\delta x^{k+n+2}}\frac{\delta^{k+n}\bar{u}}{\delta x^{k+n}}\right]\right\rangle}{\left\langle \left[\frac{\delta^{k+n}\bar{u}}{\delta x^{k+n}} - \frac{2^k(1-2^2)}{1-2^k} f c_{k,n}^{**}\Delta^2 \frac{\delta^{k+n+2}\bar{u}}{\delta x^{k+n+2}}\right]^2\right\rangle}, \tag{18}$$

substitution of which will lead to the so-called *linear dynamic finite difference approximation*. On the other hand, application of the local averaging operation to expression (16), results into a *pointwise varying* dynamic coefficient, determined as

$$c_{k,n}^{dyn} = -\frac{\mathcal{L}}{\mathcal{M}} = \frac{c_{k,n}^{*}}{1 - \frac{2^k(1-2^2)}{1-2^k}\Delta^2 f c_{k,n}^{**}\frac{\frac{\delta^{k+n+2}\bar{u}}{\delta x^{k+n+2}}\Big|^{\Delta}}{\frac{\delta^{k+n}\bar{u}}{\delta x^{k+n}}\Big|^{\Delta}}}. \tag{19}$$

Substitution of this coefficient into equation (17) leads to the *nonlinear dynamic finite difference approximation*.

Contrary to the global averaged coefficient, the local averaged coefficient is not grid independent on both grid resolutions considered, violating to some extent the mathematical foundations of the multi-resolution concept. Substitution of this coefficient into the fine resolution Taylor series will lead to the *nonlinear dynamic finite difference approximation*. Appendix A gives an overview of the higher-order derivatives in the expressions of the first and second-order dynamic approximations. In contrast to the linear dynamic scheme, the nonlinear variant is not conservative a priori, since it cannot be written straightforwardly in the divergence formulation. In Appendix B we discuss the conservative formulation of this scheme, which will be used in the further numerical study.

4. Fourier analysis

For further examination of the dynamic scheme (17) and its dynamic coefficient (16), we proceed with a Fourier analysis on the optimized finite difference approximation of the nth-order derivative. Such a Fourier analysis should allow us to better understand the quality of the constructed schemes. Remark that in case of the *nonlinear dynamic finite difference approximation* with coefficient (19) the Fourier analysis will only be valid for a single wave component and cannot be extrapolated straightforwardly to a composed wave, since superposition is not applicable to nonlinear expressions. Therefore, we perform a multiple-wave-analysis later on. In Fourier space, the nth finite difference derivative can be written as

$$\mathcal{F}\left(\frac{\delta^n \bar{u}}{\delta x^n}\right) = \left(i\kappa_n'\right)^n \mathcal{F}(\bar{u}), \tag{20}$$

with κ_n' its modified wavenumber. The modified wavenumber of a scheme can be obtained by substitution of the discrete wave $\bar{u}(x_{j+r}) = e^{i\kappa(x_j + r\Delta)}$ into the finite difference approximations and represents the error of the discrete derivatives for a single wave with wavenumber ratio κ/κ_{max}. The real part of the modified wavenumber κ_n' represents dispersion errors, while the imaginary part represent dissipation errors. We remind that the latter are absent in central schemes. The modified wavenumber of the dynamic finite difference approximation of the nth derivative is given by

$$\kappa_{n,dyn}'^{n} = \left(\kappa_n'\right)^n + c_{k,n}^{dyn}\Delta^k\left(\kappa_{n+k}'\right)^{n+k}, \tag{21}$$

in which $c_{k,n}^{dyn}$ is determined dynamically. Appendix C gives an overview of the modified wavenumber for several finite difference approximations. Obviously, the approximation of order $\mathcal{O}(\Delta^{k+2})$ is recovered if $c_{k,n}^{dyn}$ equals the theoretical value obtained from Taylor expansion. However, since $c_{k,n}^{dyn}$ is calculated by expression (16), this will generally not be the case, and the value of the coefficient $c_{k,n}^{dyn}$ will depend mainly on the instantaneous properties of the field, its derivatives and the value of f. This implies that the spectral behavior of $c_{k,n}^{dyn}$ will be crucial for the behavior of the modified wavenumber (21), and further analysis is inevitable.

4.1. The linear dynamic finite difference approximation

Since the physics of the field are reflected by the energy spectrum, an attempt is made of analyzing the behavior of the dynamic coefficient by transforming the error definition into Fourier space. Using $\hat{\cdot}$, to denote the Fourier transform, the error (8) is given in Fourier space by

$$\widehat{\mathcal{E}}(\kappa) = \widehat{\mathcal{L}} + c_{k,n}\widehat{\mathcal{M}}, \tag{22}$$

with $c_{k,n}$ the constant dynamic coefficient and

$$\widehat{\mathcal{L}}(\kappa) = c^*_{k,n}(2^k - 1)\Delta^k\left(i\kappa'_{k+n}\right)^{k+n}\hat{u}, \tag{23}$$

$$\widehat{\mathcal{M}}(\kappa) = (1-2^k)\Delta^k\left(i\kappa'_{k+n}\right)^{k+n}\hat{u} - 2^k(1-2^2)\Delta^{k+2}fc^{**}_{k,n}\left(i\kappa'_{k+n+2}\right)^{k+n+2}\hat{u}, \tag{24}$$

corresponding to Eqs. (13) and (14). We can further define the error spectrum (* denotes the complex conjugate)

$$E_{\widehat{\mathcal{E}}}(\kappa) = \widehat{\mathcal{E}}\widehat{\mathcal{E}}^* = \widehat{\mathcal{L}}\widehat{\mathcal{L}}^* + c_{k,n}\widehat{\mathcal{M}}\widehat{\mathcal{L}}^* + c_{k,n}\widehat{\mathcal{M}}^*\widehat{\mathcal{L}} + c^2_{k,n}\widehat{\mathcal{M}}\widehat{\mathcal{M}}^*. \tag{25}$$

Since the basic order of accuracy k is even for central schemes, it can be verified that in that case $\widehat{\mathcal{M}}\widehat{\mathcal{L}}^* = \widehat{\mathcal{M}}^*\widehat{\mathcal{L}}$ and thus

$$E_{\widehat{\mathcal{E}}}(\kappa) = \widehat{\mathcal{E}}\widehat{\mathcal{E}}^* = \widehat{\mathcal{L}}\widehat{\mathcal{L}}^* + 2c_{k,n}\widehat{\mathcal{M}}\widehat{\mathcal{L}}^* + c^2_{k,n}\widehat{\mathcal{M}}\widehat{\mathcal{M}}^*. \tag{26}$$

The optimal value for the coefficient $c_{k,n}$ can now be found by a least squares approximation in Fourier space, defined as

$$\frac{\partial}{\partial c_{k,n}}\int_0^{\frac{\pi}{\Delta}} E_{\widehat{\mathcal{E}}}(\kappa)\,d\kappa = 0. \tag{27}$$

Working out this integral expression leads to following expression for $c^{dyn}_{k,n}$

$$\frac{c^{dyn}_{k,n}}{c^*_{k,n}} = \frac{\displaystyle\int_0^{\frac{\pi}{\Delta}}\left(\kappa'_{k+n}\right)^{k+n}\left[\left(\kappa'_{k+n}\right)^{k+n} + \frac{2^k(1-2^2)}{1-2^k}\Delta^2 fc^{**}_{k,n}\left(\kappa'_{k+n+2}\right)^{k+n+2}\right]\hat{u}\hat{u}^*\,d\kappa}{\displaystyle\int_0^{\frac{\pi}{\Delta}}\left[\left(\kappa'_{k+n}\right)^{k+n} + \frac{2^k(1-2^2)}{1-2^k}\Delta^2 fc^{**}_{k,n}\left(\kappa'_{k+n+2}\right)^{k+n+2}\right]^2\hat{u}\hat{u}^*\,d\kappa}, \tag{28}$$

in which the product $\hat{u}\hat{u}^*$ represents the energy spectrum $E_u(\kappa)$ of the field $u(x)$. Once the shape of the energy spectrum of the field is known or a model spectrum is assumed and a value of the blending factor f is predefined, it is possible to calculate the dynamic coefficient for that spectrum from the integral expression (28). Note that the optimal value of the blending factor f will be specified later in this work. First, we assume a uniform Heaviside-like spectrum shape

$$E_u(\kappa) = 1 - H(\kappa - \kappa_c) = \begin{cases} 1, & \kappa < \kappa_c, \\ 0, & \kappa > \kappa_c, \end{cases} \tag{29}$$

in which the cutoff wavenumber κ_c indicates the highest appearing wavenumber in the field $u(x)$. Although this theoretical spectrum has no direct relation to real turbulence, it is selected in this work to examine analytically the potential of the constructed dynamic schemes. Moreover, the uniform spectrum will be used in this work for the optimization of the dispersion-relation preserving schemes, in accordance with the work of e.g. Tam and Webb [7]. The influence of assuming the real energy spectrum (28) will be demonstrated in Section 5. The simple uniform spectrum makes the expression analytically integrable, and the resulting equation describes a surface of the coefficient as function of κ_c and f. This surface is represented as a parametric plot in Fig. 1. For $f = 0$ the Taylor value $c^*_{k,n}$ is recovered, regardless of the spectral content of the field expressed by the ratio κ_c/κ_{max}. More important, for smooth signals with low ratios of κ_c/κ_{max}, the coefficient also converges to the Taylor value $c^*_{k,n}$. This means that the scheme recovers $\mathcal{O}(\Delta^{k+2})$ for very smooth signals. In case of $f \neq 0$, different profiles for $c^{dyn}_{k,n}$ as function of the filter-to-grid cutoff-ratio κ_c/κ_{max} appear. The performance is illustrated in the modified wavenumber plots of Fig. 2, where the spectral content of the field is assumed to be $\kappa_c/\kappa_{max} = 2/3$. Clearly, the linear dynamic finite difference approximation acts as an optimizable kth-order finite difference scheme, in which $c^{dyn}_{k,n}$ is obtained dynamically (for a certain f), according to the spectral content of the flow field, indicated by κ_c. As can be seen from the figures, different values of f lead to different behavior of the dynamic scheme and different accuracy. It is clear that if the ratio $0 \leqslant c^{dyn}_{k,n}/c^*_{k,n} < 1$, the scheme's Fourier characteristic will lie between that of the kth-order and $(k+2)$nd-order standard scheme, and does not result into the desired behavior. Moreover, if $c^{dyn}_{k,n}/c^*_{k,n} < 0$, i.e. $c_{k,n}$ has an opposite sign in comparison with its Taylor value $c^*_{k,n}$, poor Fourier characteristics areobserved that lie below that of the kth-order scheme. Hence, the f-values should be chosen such that $c^{dyn}_{k,n}/c^*_{k,n} \geqslant 1$ for all values of the wavenumber ratio κ_c/κ_{max}. Since $c^{dyn}_{k,n}$ acts like a sensor for the wave number content in the field $u(x)$, it should be a monotonic function of the filter-to-grid cutoff-ratio κ_c/κ_{max} such that each value of $c^{dyn}_{k,n}$ corresponds to a unique value of κ_c/κ_{max}. Both conditions are mathematically expressed by

$$\frac{c^{dyn}_{k,n}}{c^*_{k,n}} \geqslant 1, \tag{30}$$

$$\frac{1}{c^*_{k,n}}\frac{\partial c^{dyn}_{k,n}}{\partial \kappa} \geqslant 0 \quad \forall\kappa, \tag{31}$$

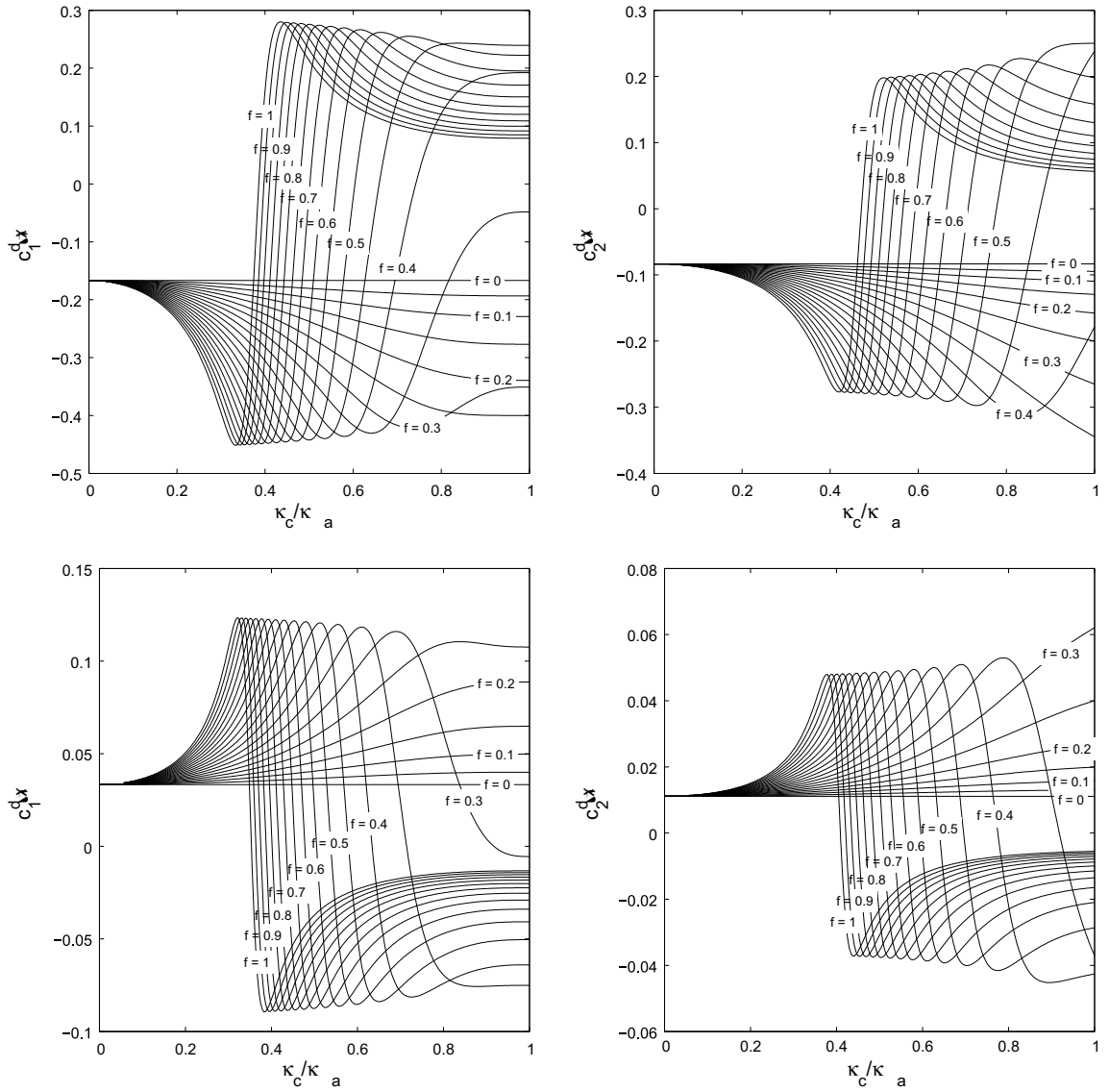

Fig. 1. *Linear dynamic scheme:* parametric plot of the dynamic coefficients c_n^{dyn} as function of cutoff wavenumber κ_c and the blending factor f. *Upper* $k = 2$, *lower* $k = 4$. *Left* $n = 1$, *right* $n = 2$.

and bound the value of f to a certain interval in which an optimal value most likely can be found. This optimal value of f will be determined in Section 5.

4.2. The nonlinear dynamic finite difference approximation

For this variant, the coefficient $c_{k,n}^{dyn}$ of the nonlinear dynamic finite difference scheme is locally averaged over half the grid spacing $\Delta/2$ such that it reduces de facto to a pointwise varying coefficient. Although the modified wavenumber for the nonlinear dynamic finite difference scheme can be determined, it will only be representative for a field $u(x)$ containing a single wave component, and is not necessarily representative for more general fields. Therefore, for general fields a multiple-wave-analysis will be performed using the transfer function. After some mathematical manipulations the single-wave Fourier expression of the resulting nonlinear dynamic coefficient (19) is found to be

$$c_{k,n}^{dyn} = \frac{c_{k,n}^{*}}{1 - \frac{2^k(1-2^2)}{1-2^k} f c_{k,n}^{**} 2(\cos(\kappa\Delta) - 1)}. \tag{32}$$

The ratio of the higher derivatives $\delta^{k+n+2}\bar{u}/\delta x^{k+n+2} / \delta^{k+n}\bar{u}/\delta x^{k+n}$ is thus represented in Fourier space by $2(\cos(\kappa\Delta) - 1)$, regardless of the values of n and k. Since this function is bounded in the interval $[-3, 0]$ for $\kappa \in [0, 2\pi/3\Delta]$, we impose the same

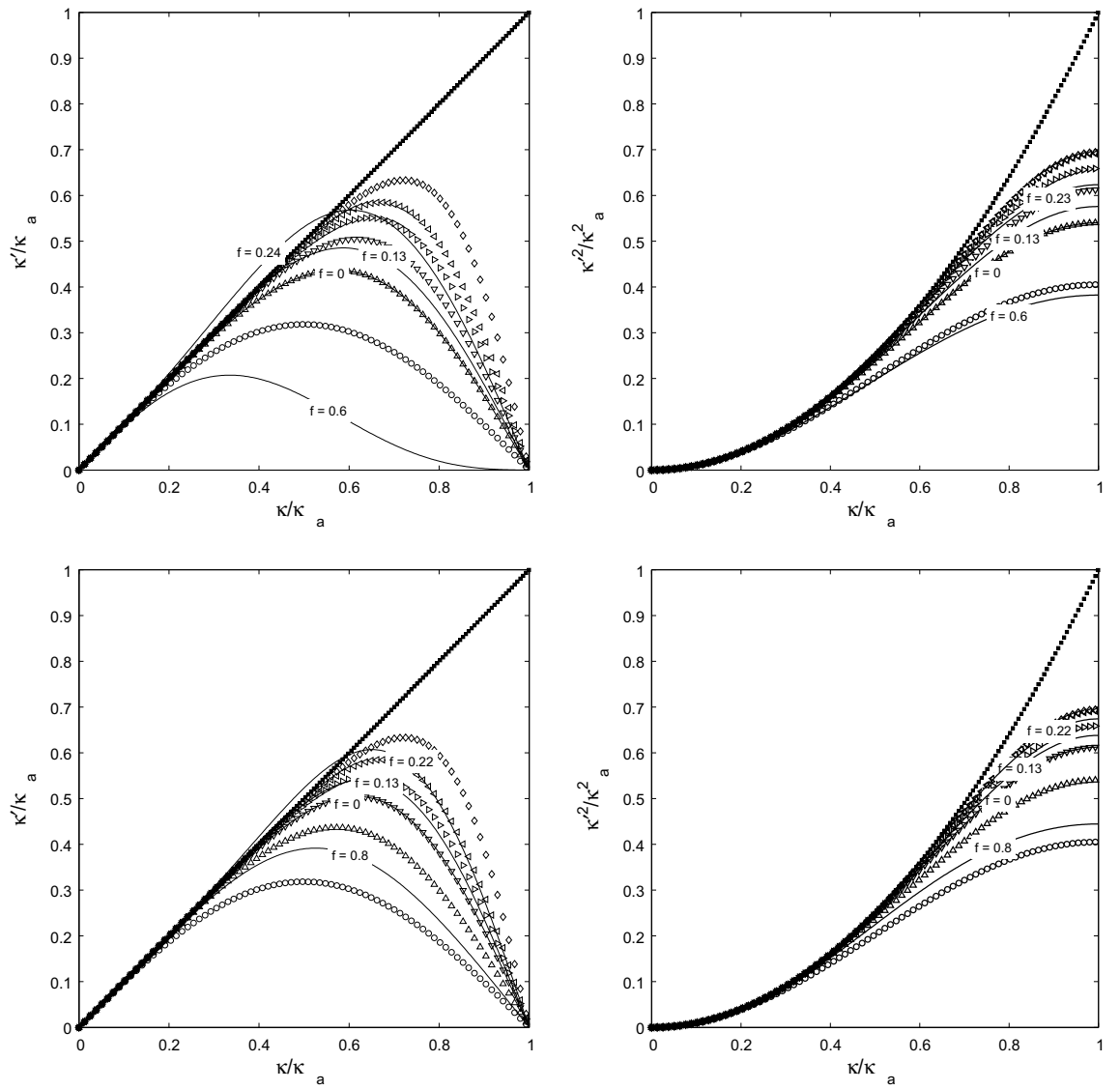

Fig. 2. *Linear dynamic scheme:* modified wavenumber for $\delta u/\delta x$ (*left*) and $\delta^2 u/\delta x^2$ (*right*), for $k = 2$ (*upper*) and $k = 4$ (*lower*). (■) spectral; (○) 2nd-order central; (△) 4th-order central; (▽) 6th-order central; (▷) 8th-order central; (◁) 10th-order central; (◇) 6th-order tridiagonal padé; (—) linear dynamic scheme.

bounds on this ratio in physical space for practical computations. This way, singularities and false values are avoided. Notice that the energy spectrum does not influence the resulting $c_{k,n}^{dyn}$, and that the value of $c_{k,n}^{dyn}$ depends only on the wavenumber κ and not on κ_c. Substitution of $c_{k,n}^{dyn}$ into Eq. (21) leads to a rational expression for the resulting modified wavenumber, in which the denominator is of the form $1 + 2\beta\cos(\kappa\Delta)$, with β a weighting coefficient. Without going into the mathematical details, we mention that it is possible to rewrite the modified wavenumber of the nonlinear dynamic scheme in the characteristic form of a tridiagonal compact Padé scheme, in which the Padé coefficients are dependent on $c_{k,n}^{*}$, $c_{k,n}^{**}$ and f. This hints to the fact that the nonlinear dynamic finite difference approximation is an explicit formulation of the tridiagonal compact scheme. When applying conditions (30) and (31) to $c_{k,n}^{dyn}$, it is easy to verify that the coefficient $c_{k,n}^{dyn}$ remains strictly negative and monotonic in the Fourier domain $0 \rightarrow \kappa_{max}$, if

$$0 \leqslant f < \frac{1-2^k}{2^{k-2}(1-2^2)c_{k,n}^{**}}. \tag{33}$$

The behavior of the dynamic coefficient, taking this limitation into account, is illustrated in Fig. 3. The coefficient $c_{k,n}^{dyn}$ is indeed monotonically decreasing with the wavenumber κ, for all the shown values of f, and displays similar behavior to that of the linear dynamic scheme. The modified wavenumber is shown in Fig. 4. It can be observed from this single-wave-analysis

that the nonlinear dynamic finite difference approximation of the derivatives can lead to highly accurate schemes, outperforming the asymptotic explicit schemes, the linear dynamic scheme and even the standard 6th-order tridiagonal Padé scheme for well chosen values of f. This is not surprising since we argued that the modified wave number of the nonlinear scheme is equivalent to that of the tridiagonal compact Padé scheme with coefficients dependent on f. Moreover, by imposing the standard constraints to obtain formal order of accuracy [21], it can be proven that for $f = 1/5$ the modified wave number reduces to that of the Padé approximant.

Although these results seem excellent, the former analysis is only valid for single-wave fields. For a more general analysis, transformation of the resulting nonlinear dynamic scheme from physical space to Fourier space would lead to complicated convolution integrals. In order to avoid this, we investigate the scheme's response to a multiple-wave field in a semi-analytical way by looking at the transfer function. Assume the multiple-wave field

$$u(\kappa, x) = \sum_{j=1}^{M} e^{(i\kappa_j x)}, \tag{34}$$

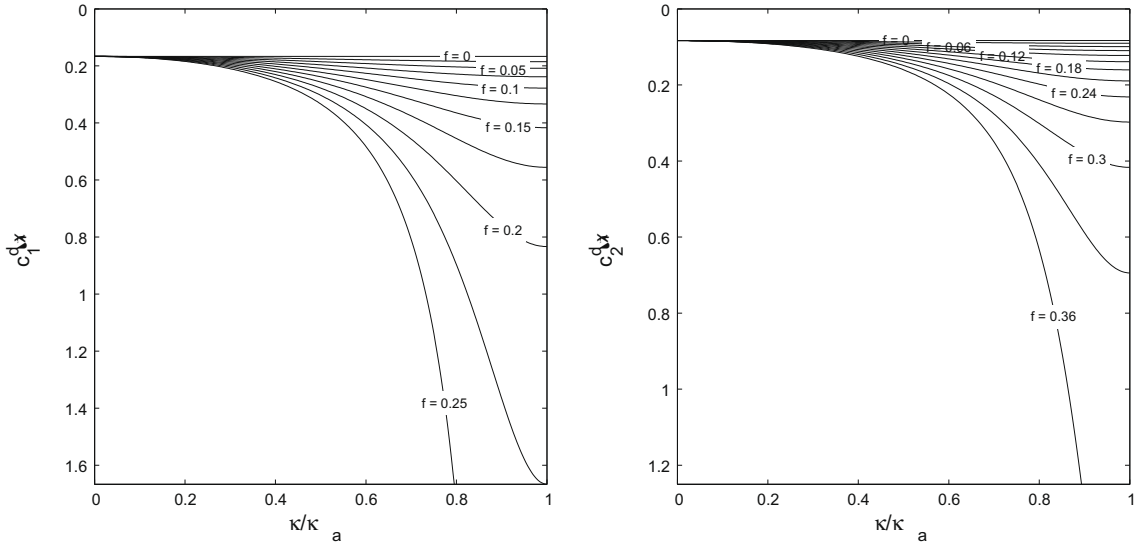

Fig. 3. *Nonlinear dynamic scheme:* parametric plot of the dynamic coefficients c_n^{dyn} as function of the wave component κ/κ_{max} and the blending factor f for $k = 2$. *Left* $n = 1$, *right* $n = 2$.

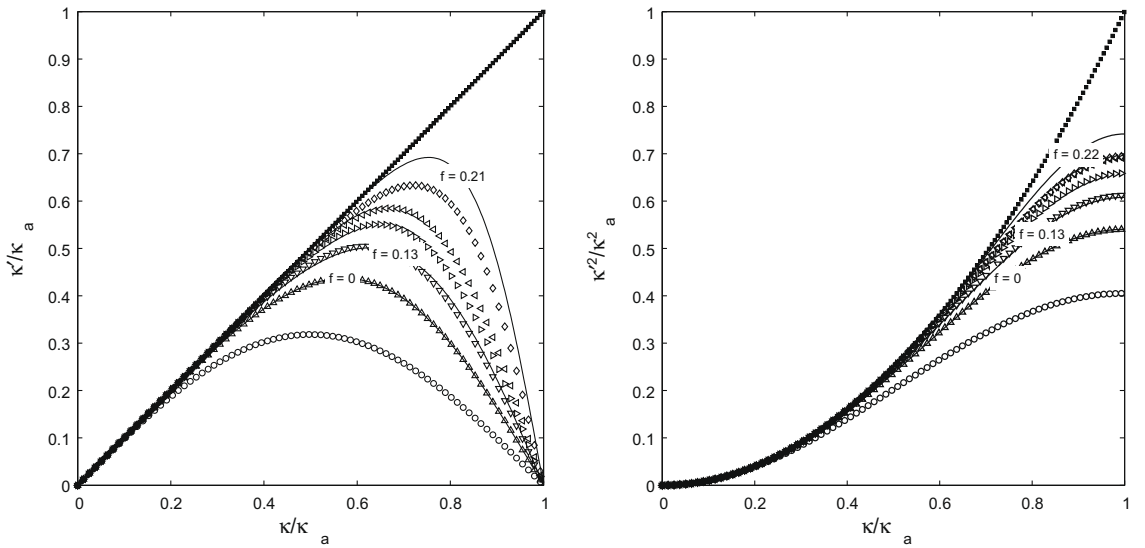

Fig. 4. *Nonlinear dynamic scheme ($k = 2$):* modified wavenumber for $\delta u/\delta x$ (*left*) and $\delta^2 u/\delta x^2$ (*right*). (■) spectral; (○) 2nd-order central; (△) 4th-order central; (▽) 6th-order central; (▷) 8th-order central; (◁) 10th-order central; (◆) 6th-order tridiagonal padé; (—) nonlinear dynamic scheme.

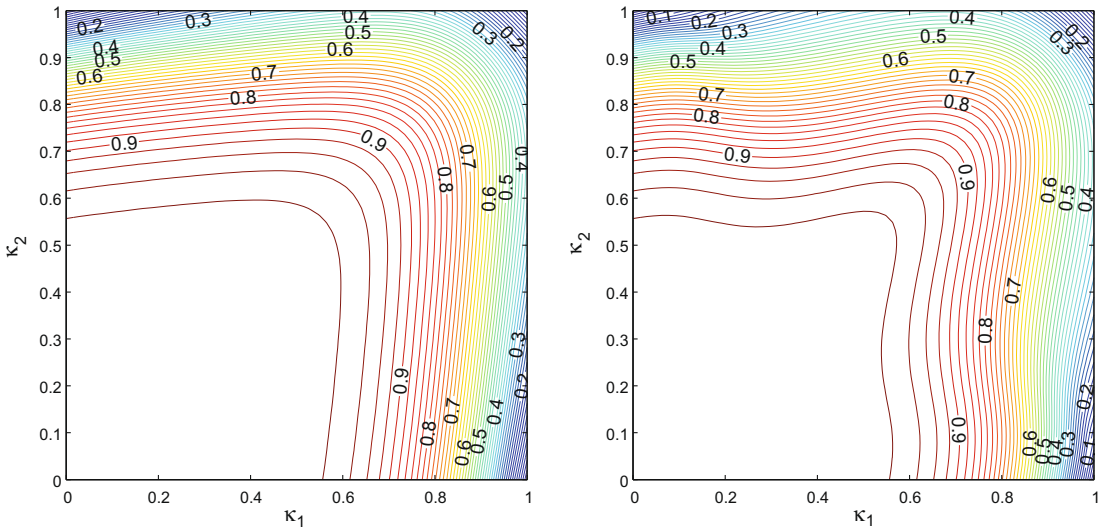

Fig. 5. *Dual-wave analysis:* transfer functions of the 6th-order tridiagonal Padé scheme (*left*) and the nonlinear dynamic scheme with $f = 1/5$ (*right*).

containing M wave components with uniformly distributed magnitude. The analytic expression of the nth-derivative is then defined as

$$\frac{\partial^n u}{\partial x^n}(\kappa, x) = \sum_{j=1}^{M} (i\kappa)^n e^{(i\kappa_j x)}. \tag{35}$$

The different wave components of the field will interact with each other in the evaluation of the nonlinear scheme. Since now we can no longer use the modified wave number to asses the performance, we define a transfer function at random position $x = x_i$, defined as

$$\mathcal{G}(\kappa) = \frac{\left|\dfrac{\delta^n \bar{u}}{\delta x^n}(\kappa, x_i)\right|}{\left|\dfrac{\partial^n u}{\partial x^n}(\kappa, x_i)\right|}, \tag{36}$$

which goes from unity to zero. We investigate the transfer function $\mathcal{G}(\kappa)$ for the case $n = 1$ and $k = 2$. Since in this case the modified wavenumber of the nonlinear dynamic scheme collapses with that of the Padé scheme when the blending factor is $f = 1/5$, we adopt this value in the evaluation of $c_{k,n}^{dyn}$. In this way comparison between the standard 6th-order tridiagonal Padé scheme and the nonlinear scheme makes the influence of nonlinear interactions clearly visible. Results are shown in Fig. 5 for a dual-wave field ($M = 2$). The general performance is in good agreement with that of the Padé scheme. However, a weak influence of the nonlinear interactions slightly affects the accuracy in the high-wavenumber region were $\kappa_j > 2/3$. Since most finite difference methods cannot represent accurately the scales for which $\kappa_j > 2/3$, this region is typically of little interest. In the current context of large-eddy simulation, these modes are eliminated through the explicit dealiasing filter in real computations. Apparently the impact of the nonlinear interactions seems to be quite limited, but further evaluation for a spectrum of waves is necessary and will be done in the numerical study.

5. Calibration of the blending factor

5.1. Procedure

In 1993, Tam and Webb [7] introduced explicit low-dispersive prefactored finite difference schemes or dispersion-relation preserving (DRP) schemes in the field of computational aeroacoustics, where qualitative simulation of propagating waves require such highly non-dispersive and non-dissipative schemes. They are constructed by an a priori least squares minimization of the dispersion error, represented by the difference between the real wavenumber and the modified wavenumber, in the wavenumber range $\kappa = 0 \rightarrow \pi/2\Delta$. Kim and Lee [8] extended this idea to implicit compact Padé schemes. Hixon [9], Ashcroft et al. [10] and Bogey and Bailly [11] also constructed similar schemes.

As mentioned before, the linear dynamic finite difference approximations behaves in a way like the dispersion-relation preserving finite difference schemes. However, in contrast to these prefactored schemes with fixed Fourier characteristics, the *linear dynamic scheme* optimizes its coefficient according to the spectral content of the flow, resulting in adaptive Fourier characteristics. This way the scheme varies between the asymptotic $(k+2)$nd-order and an optimized kth-order finite

difference approximation, depending on the spectral content on the grid and the choice of the blending factor f. The latter accentuates the sensitivity of the dynamic scheme to the spectral content of the field. Similarly, the *nonlinear dynamic finite difference scheme* can be seen as an explicit formulation of an dispersion-relation preserving Padé scheme. Here, the choice of f (which is the only degree of freedom in the dynamic schemes) determines the importance of every distinct wave component in the field.

In the current section, a natural approach is proposed for determining the optimal value of the blending factor f. The idea is to minimize the kinetic energy associated to the resulting finite difference error. This way, the energy spectrum of the flow is taken into account as a natural weighting function. Although the method is similar to the traditional methods used by e.g. Tam and Webb [7] or Kim and Lee [8], the weighting function in the current method has a clear meaning rather than being an ad-hoc function.

We define the spectral error between the exact nth derivative and its finite difference approximation as

$$\widehat{\mathcal{E}}(\kappa) = i^n\left(\kappa^n - \kappa'(\kappa,f)^n\right)\Delta^n\hat{u}, \tag{37}$$

and we define the error spectrum as

$$E_{\widehat{\mathcal{E}}}(\kappa) = \widehat{\mathcal{E}}\widehat{\mathcal{E}}^* = \left(\kappa^n - \kappa'(\kappa,f)^n\right)^2\Delta^{2n}E(\kappa), \tag{38}$$

where $E(\kappa)$ represents the generic energy spectrum of the field $u(x)$ given by the product $\hat{u}\hat{u}^*$. The optimal value for the blending factor f can be calculated by finding the minimum of the integral over all wave components, i.e. by solving

$$\frac{\partial}{\partial f}\int_0^{\frac{\pi}{\Delta}}\left(\kappa^n - \kappa'(\kappa,f)^n\right)^2 E_u(\kappa)\mathcal{W}(\kappa)\,d\kappa = 0. \tag{39}$$

If necessary an additional weighting function $\mathcal{W}(\kappa)$ can be selected to make the integrand analytically integrable [8], otherwise it should be set to unity. In the following paragraphs, the integral in (39) is solved numerically with $\mathcal{W}(\kappa) = 1$ by assuming two spectrum shapes. First, a *uniform* spectrum shape is adopted. Indeed, the uniform spectrum is most often implicitly assumed for the construction of the dispersion-relation preserving schemes, e.g. [7], and will also be used for the derivation of such schemes in this work. Moreover, the influence of the assumption of the standard uniform spectrum in comparison with other spectra will be demonstrated. Since eventually the dynamic finite difference schemes will be applied to *Burgers' turbulence* in Section 7, the energy spectra that correspond with this flows is used in order to retrieve the optimal blending factor in the dynamic finite difference approximations. The Burgers' spectrum will be termed hereafter *generic* since it may be considered representative for a wide range of *Burgers' turbulent flows*, characterized by a κ^{-2} spectrum.

5.2. Uniform spectrum

When adopting the uniform spectrum (29) for $E(\kappa)$, the integrals can be calculated analytically, leading to an expression for the optimal blending factor as function of the highest appearing wavenumber κ_c, thus $f_{opt} = f(\kappa_c)$. The values of f_{opt} obtained for the 1st and 2nd derivative for the different schemes are given in Fig. 6. Remark that the optimal value of f depends on the wavenumber range one wants to optimize for, which is indicated by κ_c. It is seen that for $\kappa_c \to 0$, the optimal blending factors tend to the value 1/5. It was found earlier that for $f = 1/5$ the modified wavenumber of the nonlinear dynamic scheme collapses with that of the standard 6th-order Padé scheme. Apparently this behavior is inherited by the linear dynamic schemes. Since very high dispersive errors exist in the range $2/3\kappa_{max} < \kappa_c < \kappa_{max}$, it is preferable that this wave number range is omitted in the optimization. Minimizing the errors in this range would be inefficient, leading to a poor overall accuracy. Moreover, in a consistent simulation, all modes in this region should be filtered out in order to prevent aliasing errors. Therefore, f_{opt} is not displayed for this high-wavenumber range.

5.3. Generic Burgers' spectrum

The adopted uniform spectrum shape makes analytical integration possible. However, the obtained optimal values for $f_{opt} = f(\kappa_c < 2/3\kappa_{max})$ are most likely suboptimal for general turbulent flows. Indeed, Kolmogorov turbulence as well as Burgers' turbulence are characterized by an energy spectrum that has an inertial range $\kappa^{-\alpha}$ with slope $-\alpha < 0$. It is possible to construct an analytical prescription as the one proposed by Pope [22] for such turbulent spectra. However, the energy containing range cannot be captured easily in a universal expression as it is dominated by the large scale flow characteristics of the specific geometry. The shape of the dissipation range is more universal, but must be expressed as function of the viscous wavenumber κ_η.

Although such a spectrum prescription could theoretically be constructed, we consider it more feasible in this work to directly use the developing energy spectrum obtained from the stored solution of a direct numerical simulation at multiple time steps. In this section we consider the DNS-solution of a 1D viscous Burgers' equation with initial velocity field $u(x) = \sin(x)$. Further details of this simulation will be given in Section 6.1. The initial sine wave evolves into a shock when advanced in time, and the spectrum develops from one single wavenumber mode to a full spectrum of modes displaying an inertial range $\kappa^{-\alpha}$ with slope $\alpha = 2$. As motivated in the introduction, optimized schemes are not that interesting in the case of, e.g. well resolved direct numerical simulations, since the smallest resolved wavenumbers contain only little energy. In order to obtain a spectrum that is more suitable for optimizing the blending factor in the dynamic schemes a priori, we filter

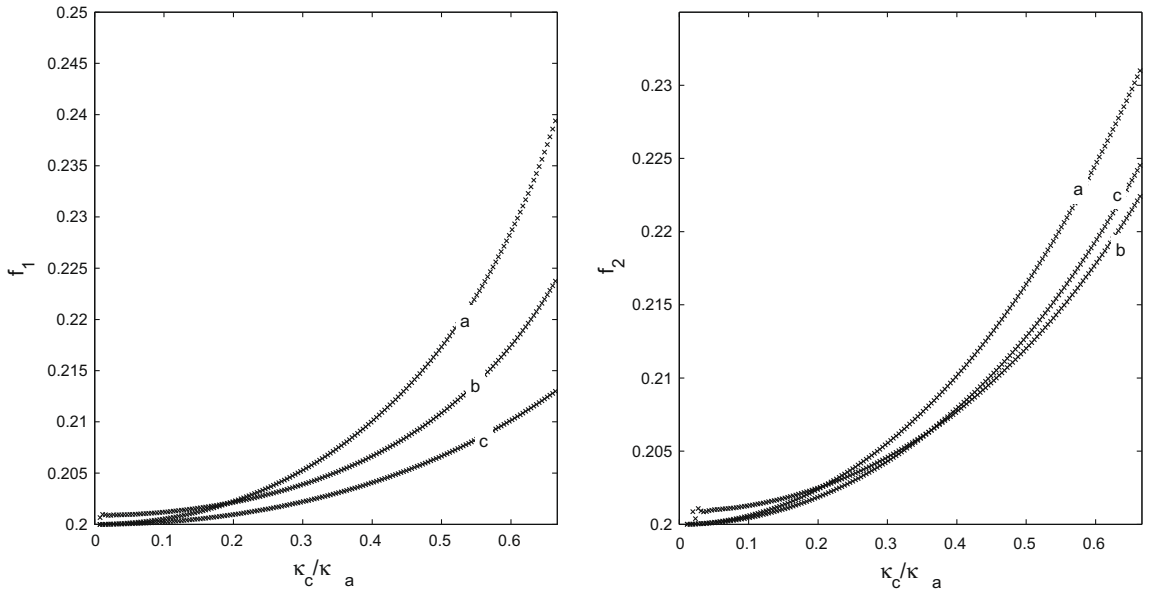

Fig. 6. *Uniform spectrum:* optimal blending factor $f_{opt} = f(\kappa_c < 2\pi/3\Delta)$ for 1st derivative (*left*) and 2nd derivative (*right*). (a) Linear dynamic scheme $k = 2$; (b) linear dynamic scheme $k = 4$ and (c) nonlinear dynamic scheme $k = 2$.

the stored DNS-solutions with a sharp Fourier filter to a certain cutoff wavenumber κ_c that lies within the inertial range for a fully developed shock spectrum. After injecting the filtered DNS-solution to a discrete grid with resolution κ_{max}, the spectrum corresponds to an ideal LES-spectrum, for which optimized schemes are relevant. We choose $\kappa_c = 2/3\kappa_{max}$. Fig. 7 shows a parametric plot of the time evolution of the normalized energy spectrum.

Assume the analytical function $E_u(\kappa, t) \propto \kappa^{-\alpha}$, which describes a general inertial range spectrum with slope $-\alpha$. A dimensionless effective wavenumber ratio can then be defined as,

$$\frac{\kappa_e(t)}{\kappa_{max}} = \left[\frac{1}{\kappa_{max}^3}\int_0^{\kappa_{max}} 3\kappa^{2+\alpha}\,\frac{E_u(\kappa,t)}{\|E_u(\kappa,t)\|}\,d\kappa\right]^{1/2}, \tag{40}$$

where the norm of the energy spectrum is defined as

$$\|E_u(\kappa,t)\| = \frac{1}{\kappa_{max}}\int_0^{\kappa_{max}} \kappa^{\alpha} E_u(\kappa,t)\,d\kappa. \tag{41}$$

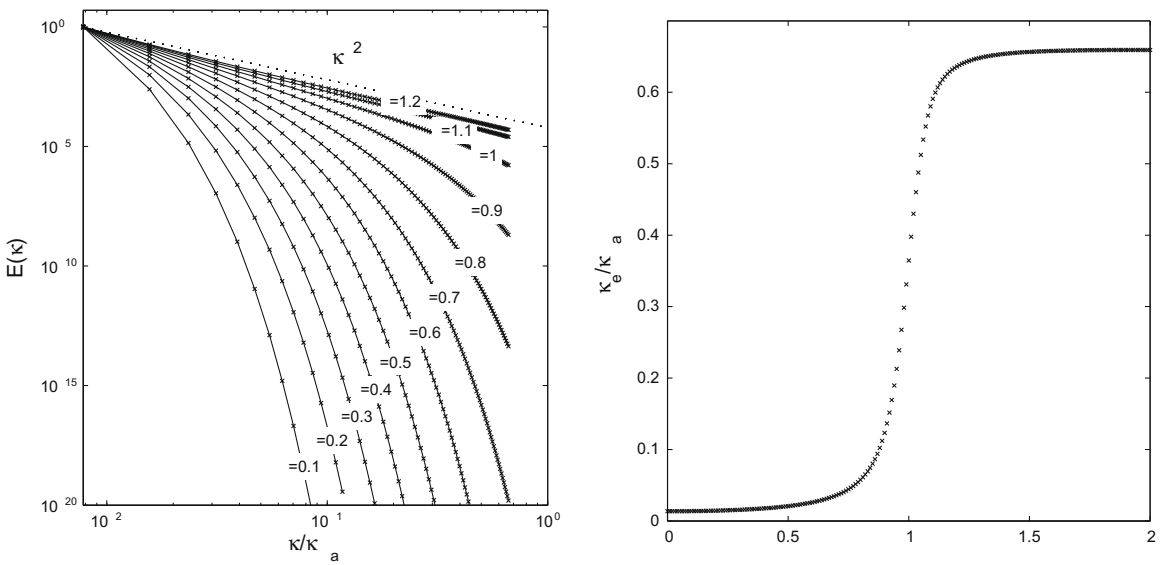

Fig. 7. *Left:* developing LES Burgers' spectrum (normalized) at different time steps. *Right:* effective wavenumber cutoff-ratio κ_e/κ_{max} as function of time.

This *ad hoc* definition, which can easily be obtained from a numerical simulation, is expected to provide a good indication about the shape of the instantaneous energy spectrum. Indeed, in case of the uniform spectrum, i.e. $\alpha = 0$, the effective wavenumber ratio reduces to

$$\frac{\kappa_e(t)}{\kappa_{max}} = \left[\frac{1}{\kappa_{max}^3}\int_0^{\kappa_c} 3\kappa^2 \frac{\kappa_{max}}{\kappa_c}\, d\kappa\right]^{1/2} = \frac{\kappa_c}{\kappa_{max}}. \tag{42}$$

It is emphasized that, unless the spectrum is uniform, the effective wavenumber κ_e does not represent exactly the highest wavenumber κ_c in the solution. Nevertheless, it provides an indication of the instantaneous spectral content of the solution on the computational grid. This is illustrated for the Burgers' equation in Fig. 7. Numerical evaluation of the integral expression (39), for each individual spectrum shape, results into an optimal value f_{opt} for the blending factor f. Calculating the effective wavenumber κ_e, that corresponds to each intermediate spectrum, allows to represent the optimal blending factors as a function of κ_e. $f_{opt} = f(\kappa_e)$ is displayed in Fig. 8. For the limit $\kappa_e \to 0$, the optimal blending factor f_{opt} tends to the same asymptotic value $f_{opt} = 1/5$ as for the uniform spectrum. Due to the creation of new wavenumber modes on the computational grid, the energy spectrum expands, and a corresponding increase of the blending factor is observed. As soon as the highest Fourier modes on the computational grid are energized, i.e. at $t \approx 0.7$ or $\kappa_e/\kappa_{max} \approx 0.05$, the filtered spectrum switches from DNS-resolution to LES-resolution and f_{opt} increases significantly. Moreover, a maximum is observed for the linear dynamic schemes in the region $0.1 \leqslant \kappa_e/\kappa_{max} \leqslant 0.3$. Once the filtered inertial range spectrum becomes fully established, i.e. at $\kappa_e/\kappa_{max} \geqslant 0.6$, the optimal blending factor of the linear dynamic schemes reaches a final value $f_{opt}(\max(\kappa_e))$. We will use this value for the practical computations. Indeed, since the fully developed inertial range spectrum is characteristic for a wide range of Burgers' flows, independent of their specific flow pattern, the corresponding $f_{opt}(\max(\kappa_e))$ can also be considered optimal for a wide range of such flows.

5.4. Dynamic vs. dispersion-relation preserving finite difference approximations

In both the *dispersion-relation preserving* schemes of e.g. Tam and Webb [7] and Kim and Lee [8], and the *dynamic* finite difference schemes presented in this work, a *predefined* parameter must be determined by using a least squares minimization over a certain wavenumber range characterized by a cutoff wavenumber κ_c.

In case of the *dynamic finite difference schemes* the optimal blending factor f_{opt}, solely determines a certain quasi-optimal *trajectory* of the dynamic coefficient $c_{k,n}^{dyn}$ as function of an a priori assumed generic shape of the fully developed inertial range spectrum as illustrated in Fig. 7. Hence, the role of f_{opt} is restricted to the calibration of the dynamic finite difference approximation for a flow at infinite Reynolds number, such that a minimal dispersion error is obtained for the fully developed inertial range spectrum. Since this predefined energy spectrum is assumed characteristic for a wide range of fully developed turbulent flows, the corresponding optimal blending factors f_{opt} are expected to be generally applicable to various numerical simulations. Once f_{opt} is defined, the dynamic finite difference scheme will optimize itself in real-time through the dynamic coefficient $c_{k,n}^{dyn}$ such that a minimal dispersion error is obtained according to the instantaneous energy spectrum of the flow. It is emphasized that this instantaneous energy spectrum may differ from the generic spectrum, used for retrieving f_{opt}. This

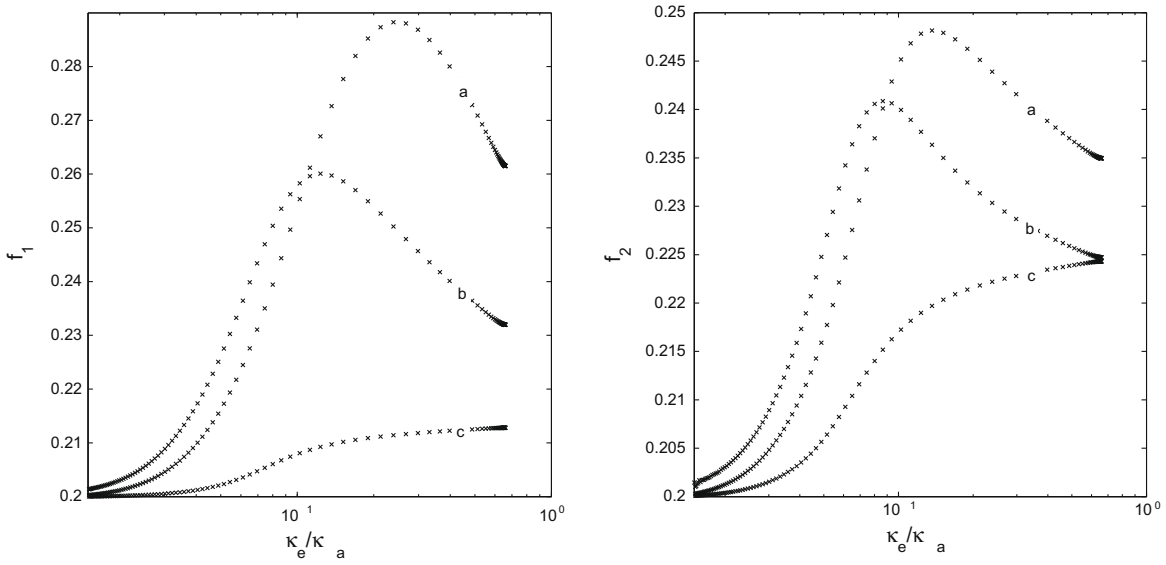

Fig. 8. *Burgers' spectrum:* optimal blending factor $f_{opt} = f(\kappa_e)$ for 1st derivative (*left*) and 2nd derivative (*right*). (a) Linear dynamic scheme $k = 2$; (b) linear dynamic scheme $k = 4$ and (c) nonlinear dynamic scheme $k = 2$.

Table 1
Uniform spectrum ($\kappa_c = 2/3\kappa_{max}$).

	Linear		Nonlinear
	$k = 2$	$k = 4$	$k = 2$
$f_{1,opt}$	0.2403148409	0.2242833402	0.2125572156
c_1^{dyn}	−0.334363121	0.0775493930	
$f_{2,opt}$	0.2314394545	0.2215576290	0.2244367639
c_2^{dyn}	−0.134556615	0.0206187300	

Table 2
Burgers' spectrum ($\kappa_e = \max(\kappa_e)$).

	Linear		Nonlinear
	$k = 2$	$k = 4$	$k = 2$
$f_{1,opt}$	0.2615500000	0.232000000	0.212800000
c_1^{dyn}	−0.301919628	0.073238344	
$f_{2,opt}$	0.2349700000	0.224720000	0.224300000
c_2^{dyn}	−0.130154404	0.020254997	

implies that the dynamic scheme has *variable* Fourier characteristics which depend on the real-time value of $c_{k,n}^{dyn}$. As a consequence, if the flow is well resolved, the dynamic schemes will return to the standard Taylor-based finite difference schemes, regardless the value f_{opt}.

In the *dispersion-relation preserving* (DRP) finite difference schemes, the optimal parameter is the constant coefficient $c_{k,n}$ itself and has to be determined by a similar least squares minimization as that used in the dynamic schemes. As a consequence, these schemes are *prefactored* and have *predefined* Fourier characteristics which are optimized for an a priori assumed shape of the energy spectrum. Typically, a uniform spectrum shape with $\kappa_c = 2/3\kappa_{max}$ is adopted for the determination of $c_{k,n}$ in the DRP schemes. It may be obvious that the value of $c_{k,n}$ used in the DRP schemes must be identical to that of the dynamic coefficient $c_{k,n}^{dyn}$ in case of a uniform spectrum, such that $c_{k,n}(\kappa_c = 2/3\kappa_{max}) = c_{k,n}^{dyn}(f_{opt}, \kappa_c = 2/3\kappa_{max})$.

The self-adaptivity of the dynamic scheme to the shape of the energy spectrum, could be advantageous in practical simulations where the position of the LES filter-cutoff is generally not known a priori. The LES-cutoff could lie in the inertial range as well as in the dissipation range corresponding to an LES or a quasi-DNS, respectively. Similar problems appear when simulating transitional flows, which display a developing spectrum and thus evolve from DNS-resolution to LES-resolution. The DRP schemes are thus suboptimal in situations that differ from those for which they are designed, as they cannot adapt to the instantaneous flow characteristics. Moreover, if the grid resolution of the LES is increased while keeping the filter width constant, DRP schemes should ideally be re-optimized to the new ratio κ_c/κ_{max}. The dynamic schemes, both linear and nonlinear, have the advantage over the DRP schemes that they automatically adapt to the changing flow conditions.

In Tables 1 and 2, the values of the optimal blending factors, that are applied in further numerical simulations, are given. Moreover, the (linear) dynamic coefficient that corresponds with this f_{opt} is shown, for a certain value of the effective wavenumber or cutoff wavenumber. Notice that for the nonlinear scheme it is meaningless to define a certain value of $c_{k,n}^{dyn}$, as it is a fluctuating field which determines a different $c_{k,n}^{dyn}$ for each wave component. Values of f_{opt} and the corresponding $c_{k,n}^{dyn}$ for the uniform spectrum with $\kappa_c = 2/3\kappa_{max}$ are given in Table 1, whereas Table 2 gives f_{opt} and the corresponding $c_{k,n}^{dyn}$ for the Burgers spectrum at $\kappa_e = \max(\kappa_e)$. As mentioned before, the above optimal values for the blending factor are used for the dynamic finite difference approximations in the numerical simulations hereafter. For the dispersion-relation preserving schemes the coefficients $c_{k,n}$ obtained with the uniform spectrum (Table 1) are used in further simulations, since they closely correspond to the original schemes of e.g. Tam and Webb [7], Kim and Lee [8] and many other authors.

The modified wavenumbers of the 2nd-order and 4th-order DRP schemes, used in the computations hereafter, collapse with that of the 2nd-order and 4th-order dynamic schemes for respectively $f_{opt} = 0.24\, f_{opt} = 0.22$, obtained with the uniform spectrum at $\kappa_c = 2/3\kappa_{max}$. These modified wavenumbers were already presented in the theoretical analysis in Fig. 2.

6. Numerical setup

For a first evaluation of the developed schemes for large-eddy simulation, it may be more useful to consider a simpler problem than LES of three-dimensional Navier–Stokes turbulence. Following the work of Love [23] and Das and Moser [24], we select the one-dimensional viscous Burgers' equation. Similar to the Navier–Stokes equations, Burgers' equation contains a quadratic nonlinear term which is responsible for the generation of small scale structures. These small scales are eventually dissipated by a viscous force. Moreover, the energy spectrum of the viscous Burgers' equation is characterized by an *inertial range*, through which energy is transferred from the large scales to the small scales until it is dissipated by the viscosity in the *dissipation range*. Since this process is similar to that of the Navier–Stokes equations, Burgers [25] proposed his equation as a simplified model for turbulence. Despite the agreements, the small scale dynamics of Burgers' turbulence

and real turbulence are substantially different. In Burgers' turbulence, the small scales represent shock waves, with thickness in the order of the viscous scale. Instead of a successive breakdown of the large vortex structures into smaller ones as in real turbulence, the small structures tend to merge into large ones. The corresponding inertial range scaling for a shock wave spectrum is found to be κ^{-2}. Nevertheless, since in Burgers' model turbulence the large and small scales are separated in Fourier space by a characteristic inertial range κ^{-2} and are thus statistically independent, it is considered as a very useful tool, not only for investigating the influence of the subgrid modeling, but also for assessing the quality of the proposed dynamic finite difference approximations in an large-eddy simulation environment.

The viscous Burgers' equation in non-dimensional form is given by

$$\frac{\partial u}{\partial t}+\frac{1}{2}\frac{\partial u^2}{\partial x}=\frac{1}{Re}\frac{\partial^2 u}{\partial x^2}, \tag{43}$$

subjected to the periodic boundary conditions in the domain $0 \leqslant x \leqslant 2\pi$

$$u(x,t)=u(x+2\pi,t). \tag{44}$$

The initial condition

$$u(x,0)=\sin(x) \tag{45}$$

is imposed at $t=0$, representing a single Fouriermode. The Reynolds number is set to $Re=1/\nu=500$. The initial kinetic energy and dissipation rate can be calculated as

$$k(t=0)=\int_0^{\kappa_\eta} E(\kappa,t=0)\,d\kappa=\frac{1}{2\pi}\int_0^{2\pi}\frac{1}{2}[u(x,t=0)]^2\,dx=\frac{1}{4}, \tag{46}$$

$$\varepsilon(t=0)=2\nu\int_0^{\kappa_\eta}\kappa^{-2}E(\kappa,t=0)\,d\kappa=\frac{\nu}{\pi}\int_0^{2\pi}\left[\frac{\partial u}{\partial x}(x,t=0)\right]^2 dx=\frac{1}{Re}. \tag{47}$$

For $t>0$, the single wave evolves in time and finally runs into a stationary shock at $x=\pi$, which is damped by viscous forces. Therefore, the test case be seen from a numerical point of view as the 1D equivalent of the Taylor–Green transitional flow. As mentioned before, the corresponding shock wave energy spectrum exhibits an inertial range κ^{-2}, through which energy is transferred from the large scales to the small scales, and finally dissipated by viscous effects.

6.1. Direct numerical simulation of the Burgers' equation

First, a reference solution for the Burgers' system is generated from a direct numerical simulation. A uniform grid is adopted with $n_x=8192$ nodes, for which the grid cutoff-wavenumber $\kappa_{max}=\pi/\Delta_{DNS}=4096$, such that all scales in the dissipation range, including the viscous scale $\kappa_\eta=\pi\varepsilon^{1/4}/\nu^{3/4}$ are well resolved at all times (see Fig. 9). Indeed, the viscous wavenumber reaches a maximum of $\kappa_\eta\approx 355$ at maximum dissipation, which is far below the grid cutoff-wavenumber κ_{max}. The simulation is done using a pseudo-spectral code, avoiding numerical discretization errors. Dealiasing is not required, since the viscous scale is fully resolved, and consequently no aliasing error can appear. The nonlinear term is discretized in the energy conserving skew-symmetric form.

The standard 4-stage Runge–Kutta time-stepping with coefficients $[1/4,1/3,1/2,1]$ is adopted. The time step is set to $\Delta t=1.10^{-5}$ such that CFL number $\mathrm{CFL}\leqslant \Delta t\max(u)/\Delta_{DNS}\leqslant 1.3\cdot 10^{-2}$ and the Neumann number $Neu=2\nu\Delta t/\Delta_{DNS}^2\approx 6.8\cdot 10^{-2}$. The decaying shock wave is followed until $t=10$. Simulation results of $u(x,t=t_j)$ and the corresponding spectrum are illustrated in Fig. 9.

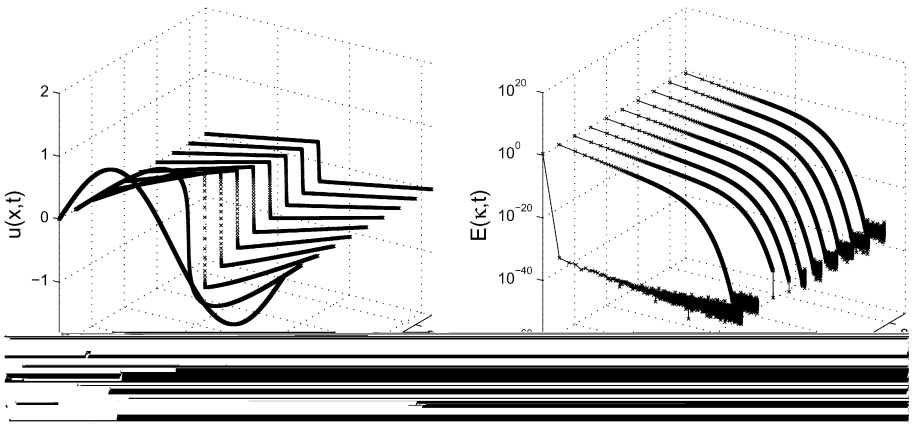

Fig. 9. *Burgers' equation.* Velocity field $u(x,t)$ (*left*). Energy spectrum $E(\kappa,t)$ (*right*).

6.2. Large-eddy simulation of the Burgers' equation

The goal of LES is to reproduce the dynamics of the filtered DNS-solution, by resolving only the high energetic large scale features (low wavenumbers) in the flow, corresponding to ideally 80% of the total kinetic energy [22], while neglecting the low energetic small scales (high-wavenumbers). This requires the definition of an appropriate spatial filter. In this work, a sharp spectral Fourier filter is used. Although there are ongoing discussions favoring smooth filters over the sharp cutoff filter and vice versa [26–28], here we prefer the sharp Fourier filter to obtain a clear scale separation in wavenumber space, eliminating modes above the cutoff but leaving modes below the cutoff unharmed. This is in contrast with smooth filters where small scales are only damped, but not eliminated. Thus, from a mathematical point of view, only the sharp Fourier filter guarantees no aliasing after discretization. Moreover, subgrid and supergrid issues are clearly separated, and no subfilter scales have to be modeled. Inevitably, when using sharp Fourier filters, the Gibbs-phenomenon arises, due to the truncation of an infinite Fourier series. Although elimination of the wiggles is subject to shock capturing schemes (TVD, MUSCL, ENO), they are part of the filtered solution in the context of LES [24]. Note also that the current testcase is quite different from the testcases generally used in the development of DRP schemes, where either linear wave propagation problems are studied [8,10,18], or the simulation of the inviscid nonlinear Burgers' equation, without dealiasing nor subgrid dissipation [9].

Applying a sharp Fourier filter with cutoff $\kappa_c = \pi/\Delta_f$ to the continuous Eq. (43), denoting $\widetilde{\cdot}$ as the filtered quantity, gives

$$\frac{\partial \widetilde{u}}{\partial t} + \frac{1}{2}\frac{\partial \widetilde{\widetilde{u}\widetilde{u}}}{\partial x} = \frac{1}{Re}\frac{\partial^2 \widetilde{u}}{\partial x^2} - \frac{1}{2}\frac{\partial \tau}{\partial x}, \tag{48}$$

in which the subgrid stress is defined as

$$\tau = \widetilde{u\widetilde{u}} - \widetilde{\widetilde{u}\widetilde{u}}. \tag{49}$$

The nonlinear term is explicitly filtered in order to avoid aliasing [4,29]. Now the equation can be discretized from continuum space $\mathbb{R}$ to the discrete space with grid resolution $\kappa_{max} = \pi/\Delta$, leading to

$$\frac{\delta \tilde{u}}{\delta t} + \frac{1}{3}\widetilde{\tilde{u}\frac{\delta \tilde{u}}{\delta x}} + \frac{1}{3}\frac{\delta \widetilde{\tilde{u}\tilde{u}}}{\delta x} = \frac{1}{Re}\frac{\delta^2 \tilde{u}}{\delta x^2} - \frac{1}{2}\frac{\delta \tau}{\delta x}. \tag{50}$$

Following the work of De Stefano and Vasilyev [26], the nonlinear term is discretized in the skew-symmetric formulation in order to guarantee the discrete conservation of kinetic energy. This is recommended for large-eddy simulation, and is considered more important than the a priori conservation of momentum. Following the work of Orszag [4] we adopt $\kappa_c = 2/3\kappa_{max}$. Since Eqs. (48) and (50) are unclosed, an appropriate subgrid-scale model is needed to close the equations. Two models are considered in this work: *the perfect subgrid-scale model* and a *dynamic Smagorinsky model*. In case of the *perfect subgrid-scale model*, the exact subgrid-stresses are extracted at each Runge–Kutta step from a simultaneous running DNS-simulation. This results in a perfect LES in which the filtered DNS results are recovered exactly in case of exact numerics. For the *dynamic Smagorinsky model* we follow the work of Love [23] defining the dealiased subgrid-scale closure as

$$\tau = -2\widetilde{\nu_t \frac{\delta \tilde{u}}{\delta x}}, \tag{51}$$

in which the turbulent viscosity

$$\nu_t = C^2 \Delta_f^2 \left\langle \left| \frac{\delta \tilde{u}}{\delta x} \right| \right\rangle_w. \tag{52}$$

$\langle\cdot\rangle_w$ denotes the average over a length w. The filter width is chosen $\Delta_f = \Delta$. In the limit $w \to \Delta$, (52) tends to the one-dimensional equivalent of the Smagorinsky model, while $w \to L$ tends to the direct-interaction subgrid model investigated by Leslie and Quarini [30]. Here, we choose $w = L$ because it was found to lead to better results. Since the subgrid dissipation should only start when the nonlinear terms begin to produce wavenumbers not visible on the LES grid, Germano's dynamic procedure [31] is used to calculate the appropriate value of C^2. Appendix D explains in more detail Germano's dynamic procedure applied to the Burgers' equation.

The large-eddy simulation of the Burgers' equation is done on a uniform mesh with $n_x = 256$ nodes, for which the grid resolution is $\kappa_{max} = \pi/\Delta = 128$ and the physical resolution is defined by the filter $\kappa_c = 2/3\kappa_{max} = 85$. Different central finite difference discretizations are investigated, among which the dispersion-relation preserving schemes and the dynamic low-dispersive schemes. For the latter family of schemes, some particularities arise. Since $\tilde{u}$ and $\tilde{u}\tilde{u}$ have strongly different energy spectra, the dynamic coefficients $c_{k,n}^{dyn}$ are different in the *linear* dynamic finite difference approximations of the advective and convective contributions in (48). Hence, skew-symmetry and the conservation of kinetic energy are lost. In order to preserve skew-symmetry the same dynamic coefficient $c_{k,n}^{dyn}$ should be used in both contributions. It would theoretically be possible to include both the convective and advective operator in the expressions (13) and (14), resulting in

$$\mathcal{L} = c_{k,n}^{*}(2^k - 1)\Delta^k \left\{ \left| \widetilde{\tilde{u}\frac{\delta^{k+n}\tilde{u}}{\delta x^{k+n}}} \right|^{\Delta} + \left| \frac{\delta^{k+n}\widetilde{\tilde{u}\tilde{u}}}{\delta x^{k+n}} \right|^{\Delta} \right\}, \tag{53}$$

$$\mathcal{M} = (1-2^k)\Delta^k \left\{ \tilde{u} \frac{\widetilde{\delta^{k+n}\tilde{u}}}{\delta x^{k+n}}\Big|^{\Delta} + \frac{\delta^{k+n}\widetilde{\tilde{u}\tilde{u}}}{\delta x^{k+n}}\Big|^{\Delta} \right\} - 2^k \Delta^k f c^{**}_{k,n} (1-2^2)\Delta^2 \left\{ \tilde{u} \frac{\widetilde{\delta^{k+n+2}\tilde{u}}}{\delta x^{k+n+2}}\Big|^{\Delta} + \frac{\delta^{k+n+2}\widetilde{\tilde{u}\tilde{u}}}{\delta x^{k+n+2}}\Big|^{\Delta} \right\}, \tag{54}$$

and leading to a single dynamic coefficient for the skew-symmetric operator. Instead an alternative method is used, in which the dynamic coefficient $c^{dyn}_{k,n}$ obtained for $\delta\tilde{u}/\delta x$ is used in the evaluation of $\delta\widetilde{\tilde{u}\tilde{u}}/\delta x$. We prefer the latter method in this work, since it is equivalent to the discretization of the skew-symmetric operator using traditional standard schemes or prefactored optimized schemes. In case of the *perfect subgrid-scale model* the same dynamic coefficient $c^{dyn}_{k,n}$ is used for the discretization of the subgrid force $\delta\tau/\delta x$ as for the skew-symmetric operator. However, since the subgrid force of the *eddy-viscosity model* is discretized analogously to the molecular viscous term, the dynamic coefficient $c^{dyn}_{k,n}$ of the 2nd derivative is used. For the *non-linear* dynamic scheme, $c^{dyn}_{k,n}$ depends theoretically neither on $\tilde{u}$ or $\tilde{u}\tilde{u}$, as it is an explicit approximation of the dispersion-relation preserving Padé scheme. Therefore, the advective and convective contributions are calculated straightforwardly using the conservative formulation of the nonlinear dynamic scheme (Appendix B). Finally, because higher wavenumber modes are generated by the nonlinear finite difference approximations, every Runge–Kutta step the updated velocity field $u(x)$ is filtered with the dealiasing filter instead of only to the nonlinear term in equation (48).

7. Numerical results

After defining an appropriate error evaluation, a priori tests are done on a filtered DNS-solution. The numerical errors on the solution of a large-eddy simulation of Burgers' equation are investigated as well as their interactions with the modeling errors.

7.1. Quantification of numerical errors

To quantify numerical errors due to finite difference approximations, we use the error decomposition as defined by Vreman et al. [19] and Meyers et al. [20], which tries to separate modeling errors from numerical errors. Consider a reference DNS containing the viscous scale κ_η, and a specific flow variable of interest ϕ. The total error in ϕ for a large-eddy simulation with grid resolution $\kappa_{max} = \pi/\Delta$ and filter resolution $\kappa_c = \pi/\Delta_f$ is then defined as

$$\varepsilon_{\phi,total}(\kappa_c, \kappa_{max}) = \phi_s\big(\kappa_\eta, \widetilde{3/2}\kappa_\eta\big) - \tilde{\phi}_{fd}(\kappa_c, \kappa_{max}). \tag{55}$$

The error is explicitly defined as function of the LES filter resolution and grid resolution where $\phi_s(\kappa_\eta, \widetilde{3/2}\kappa_\eta)$ represents the filtered *spectral* DNS-solution, while $\tilde{\phi}_{fd}(\kappa_c, \kappa_{max})$ represents the *finite difference* LES-solution with cutoff κ_c on an LES grid with maximum wavenumber κ_{max}. The total error consists of contributions of numerical errors and modeling errors and is decomposed as

$$\varepsilon_{\phi,model}(\kappa_c, \kappa_{max}) = \phi_s\big(\kappa_\eta, \widetilde{3/2}\kappa_\eta\big) - \tilde{\phi}_s(\kappa_c, \kappa_{max}), \tag{56}$$

$$\varepsilon_{\phi,num}(\kappa_c, \kappa_{max}) = \tilde{\phi}_s(\kappa_c, \kappa_{max}) - \tilde{\phi}_{fd}(\kappa_c, \kappa_{max}). \tag{57}$$

$\tilde{\phi}_s(\kappa_c, \kappa_{max})$ represents the *spectral* LES-solution with cutoff κ_c and numerical resolution κ_{max} corresponding to an LES grid, and would be equivalent with $\tilde{\phi}_{fd}(\kappa_c, \kappa_\infty)$ which is the finite difference LES-solution on an infinitely fine grid. The modeling error, $\varepsilon_{\phi,model}$ is related to the adopted subgrid closure, while the numerical error $\varepsilon_{\phi,num}$ contains aliasing errors as well as discretization errors. In case of proper dealiasing through explicit filtering, $\varepsilon_{\phi,num}$ reduces exactly to the finite difference discretization errors. Although $\varepsilon_{\phi,num}$ is well defined for a perfect subgrid model or a static Smagorinsky model in which the value of the theoretical constant C^2 is chosen a priori, the errors are not clearly separated in case of a dynamic model where the value of model coefficient C^2 is affected by the numerics. In the latter case numerical errors and modeling errors continuously interfere through the feedback of the numerically obtained dynamic model constant C^2. In this work, we attempt to show the influence of the numerics on the calculation of the dynamic model coefficient.

Since the value of the model coefficient C^2 is considered to be a *theoretical* model parameter that corresponds to the instantaneous energy spectrum of the resolved velocity field, also the dynamic procedure by which it is determined, might be considered as a separate post-processing procedure at each time step. Hence, in this work, we attempt to separate the discretization of the LES-equations and that of the dynamic procedure. Then, three coefficients can be distinguished. First the coefficient $C_{s,s}$ denotes the theoretical value that is obtained by applying the dynamic procedure, in which the derivatives are evaluated spectrally, to the solution of the pseudo-spectral large-eddy simulation of Burgers' equation. Further the coefficient $C_{s,fd}$ is defined, which represents the theoretical value that is obtained by applying the dynamic procedure, in which the derivatives are also evaluated spectrally, to the solution of the finite difference large-eddy simulation of Burgers' equation. Although $C_{s,fd}$ is affected by the finite difference errors in the LES-solution due to the discretization of the basic LES equation, its calculation is not liable to finite difference errors. Hence, this allows to isolate more or less the influence of the numerical errors in the Burgers' solution on the model coefficient. Finally, $C_{fd,fd}$ denotes the finite difference approximation of the theoretical value $C_{s,fd}$. This coefficient is obtained in a finite difference large-eddy simulation of Burgers' equation in which the derivatives within dynamic procedure are also evaluated with the same finite difference method. In summary,

both coefficients $C_{s,fd}$ and $C_{fd,fd}$ contain influences of the discretization of the LES-equations, however $C_{s,fd}$ does not suffer from discretizations in its calculation, in contrast to $C_{fd,fd}$. The influence of both coefficients will be shown in the next paragraph.

The decomposed errors, i.e. the modeling error and the numerical error, can now be evaluated in two different ways leading to mathematics-based and physics-based error definitions. Following the work of Chow and Moin [3], we first select the velocity field $u(x)$ (or its derivative in case of a priori studies) as the variable of interest ϕ. The corresponding energy spectrum and the global magnitude of the pointwise errors ε_u are then calculated as

$$E_\phi(\kappa) = \widehat{\varepsilon_u}(\kappa)\widehat{\varepsilon_u}^*(-\kappa), \quad \phi = \varepsilon_u, \tag{58}$$

$$k_\phi = \int_0^{\kappa_{max}} E_{\varepsilon_u}(\kappa)d\kappa, \quad \phi = \varepsilon_u. \tag{59}$$

Remark that the magnitude k_ϕ, ε_u corresponds to the L_2-norm, often used in error evaluation, by the relation $L_2 = 2\pi\sqrt{k_\phi}$, and this error always has a positive sign. We call this type of error definition the mathematics-based error.

The alternative is to select the weighted energy spectrum of the field $\kappa^p E_u(\kappa)$ as the variable of interest ϕ. For low values of p the large scale errors are dominant, while small scale errors are accentuated, for increasing p. The corresponding error definition leads to the error between the energy spectra ε_E, the total error on the kinetic energy ε_k if $p = 0$ and the total error on the dissipation ε_ε if $p = 2$

$$\varepsilon_E(\kappa) = \Delta E_u(\kappa), \tag{60}$$

$$\varepsilon_k = \Delta k = \int_0^{\kappa_{max}} \Delta E_u(\kappa)\, d\kappa, \tag{61}$$

$$\varepsilon_\varepsilon = \Delta \varepsilon = \int_0^{\kappa_{max}} \kappa^2 \Delta E_u(\kappa)\, d\kappa. \tag{62}$$

This alternative method, used, e.g. in the work of Meyers et al. [20], Park and Mahesh [5] and Berland et al. [6], differs from the previous method in the sense that the errors are evaluated in a physics-based manner instead of a mathematics-based manner. Park and Mahesh [5] defined the instantaneous error on the energy spectrum as a *static error analysis* whereas they termed the time-dependent global errors on the kinetic energy or dissipation as a *dynamic error analysis*. Remark further that the sign of ε_k and ε_ε could be either positive or negative, enabling to see interactions between different errors. The physics-based error definitions represent only errors on the amplitude of the solution, assumed that the influence of phase is not accumulated in time. Instead, the mathematics-based error contains contributions of both amplitude and phase errors of the solution at a certain time. Meyers et al. [32] found that some physics-based error definitions may lead to an overly optimistic accuracy, which is confirmed by our numerical results. Hence, mathematics-based error definitions are more strict as they contain information about phase and amplitude. These error definitions are used for analyzing the performance of finite difference schemes, and interactions with the subgrid model.

7.2. A priori results

Table 3 gives an overview of the performed simulations, and the corresponding symbol notation used in the plots to follow. First, the performance of the linear ($k = 2, 4$) and nonlinear ($k = 2$) dynamic schemes is investigated in an a priori way. The dynamic finite difference approximations of the first derivative $\delta u/\delta x$ are calculated from the filtered DNS-solution at every time step, and their performance is compared to the standard central schemes and the dispersion-relation preserving schemes (DRP) of Tam and Webb [7]. The error is thus $\varepsilon_{dudx} = \partial u/\partial x - \delta u/\delta x$. Only the mathematics-based error definition using the energy spectrum of the error $E_\phi(\kappa, t), \phi = \varepsilon_{dudx}$ and the global kinetic energy of the error $k_\phi, \phi = \varepsilon_{dudx}$ are considered in this a priori study. As mentioned before, the latter is related to the L_2-norm by $L_2 = 2\pi\sqrt{k_\phi}$. Fig. 10 presents k_ϕ as function of time. At the early stages of the simulation, when the spectrum is still developing and the small scales contain little or no energy, the linear dynamic schemes with $k = 2, 4$ almost collapse with the asymptotic 4th-, respectively, 6th-order standard central schemes. This is in contrast to the equivalent 2nd- and 4th-order DRP schemes which reach only 2nd-, respectively, 4th-order accuracy. When the flow evolves, the linear dynamic schemes adapt according to the developing energy spectrum. Once the shock is formed resulting in an inertial range spectrum, the linear dynamic schemes act like the DRP schemes and

Table 3
Overview of the different simulations. Note that the 2nd- and 4th-order DRP schemes and the 4th-order tridiagonal DRP Padé are equivalent with both linear, respectively nonlinear dynamic schemes with fixed constant coefficients $c_{k,n}$ calculated in Table 1.

Symbols – simulations			
○	2nd-order central	•	2nd-order DRP
△	4th-order central	▲	4th-order DRP
▽	6th-order central	■	4th-order tridiagonal DRP Padé
▷	8th-order central	—	Linear dynamic scheme with $k = 2$
◁	10th-order central	– – –	Linear dynamic scheme with $k = 4$
□	6th-order tridiagonal Padé	–·–·	Nonlinear dynamic scheme with $k = 2$

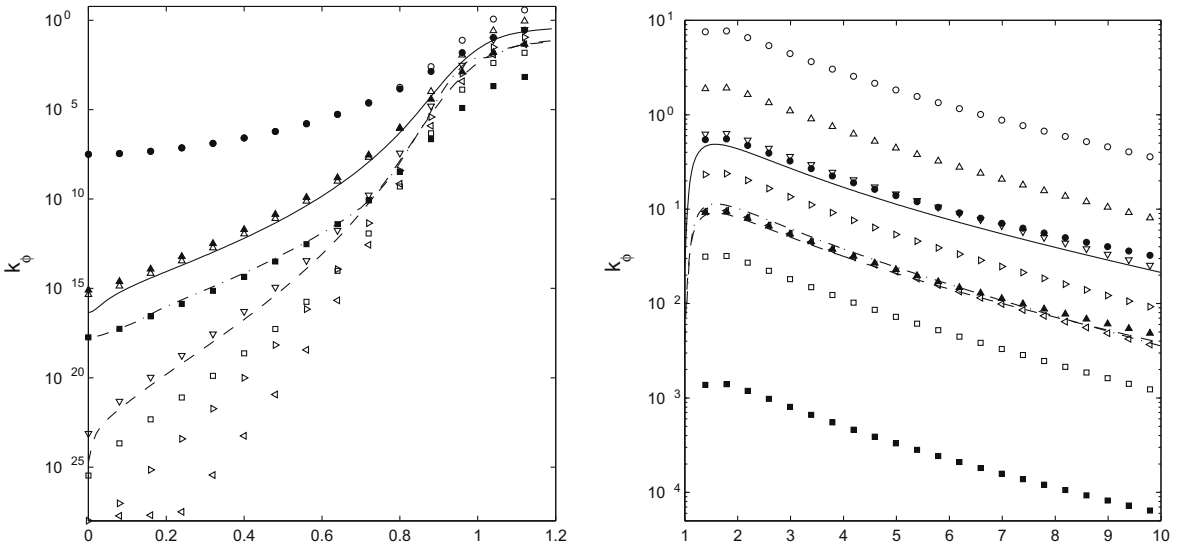

Fig. 10. *A priori results:* magnitude of the error on the 1st derivative $k_\phi, \phi = \varepsilon_{dudx}$ before shock formation at $0 \leqslant t \leqslant 1.2$ (*left*) and after shock formation and during the decay at $1 \leqslant t \leqslant 10$ (*right*). (Symbols see Table 3.)

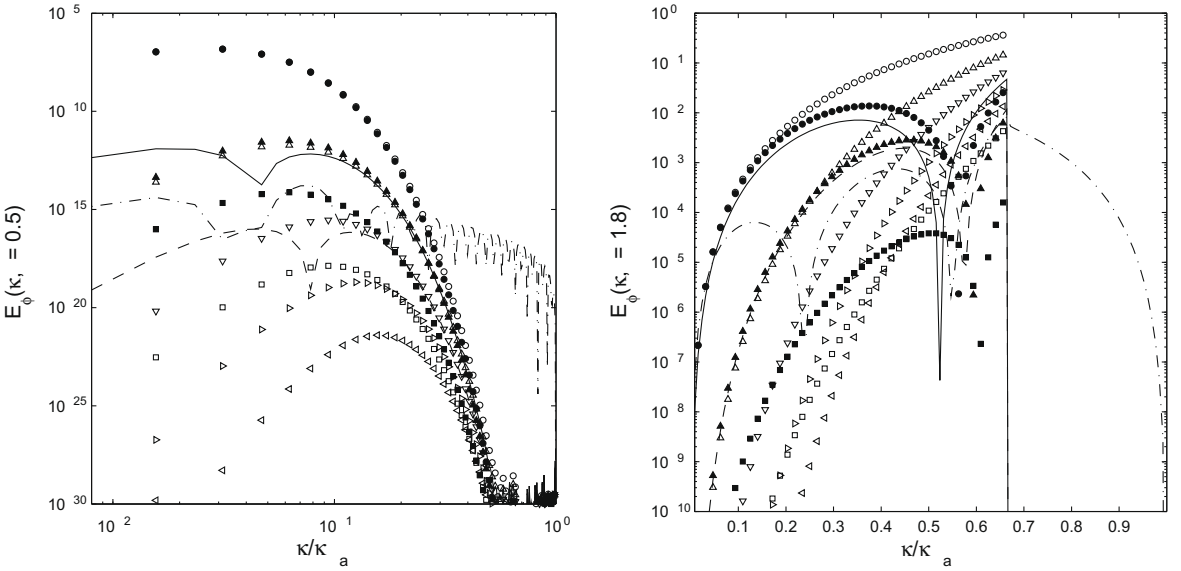

Fig. 11. *A priori results:* snapshots of the energy spectrum of the error on the 1st derivative $E_\phi(\kappa, t), \phi = \varepsilon_{dudx}$ at times $t = 0.5$ (developing spectrum) (*left*) and $t = 1.8$ (fully developed spectrum) (*right*). (Symbols see Table 3.)

obtain high accuracy. The linear dynamic scheme with $k = 2$ obtains a better accuracy than the standard 6th-order schemes, while the accuracy of the dynamic scheme with $k = 4$ reaches that of the 10th-order central scheme. For the decaying shock wave, which is accompanied by a shrinkage of the energy spectrum, the linear dynamic schemes tend toward their initial behavior with formal order of accuracy. These findings are confirmed by Fig. 11 which displays a snapshot of the energy spectrum $E_\phi(\kappa, t), \phi = \varepsilon_{dudx}$ at times $t = 0.5$ (before shock formation), and $t = 1.8$ (after shock formation) near maximum dissipation. Hence, the energy spectra of the velocity field E_u differ significantly at both time steps. At $t = 0.5$ the linear dynamic schemes reduce almost to the asymptotic 4th-, respectively, 6th-order schemes. Clearly, they are optimized for the lower wavenumber modes which contain most of the energy. This is in contrast to the equivalent DRP schemes which are calibrated for a full spectrum and therefore reach only 2nd-, respectively, 4th-order accuracy. At $t = 1.8$ the spectrum is fully developed and the linear dynamic schemes have adapted accordingly. The same accuracy as the 2nd-, respectively, 4th-order scheme is obtained for the low wavenumber region, while the error on the high-wavenumber modes is significantly reduced

compared to the traditional central schemes. As expected, similar performance for the DRP schemes is observed here. To illustrate the adaptivity of the linear dynamic scheme, Fig. 12 gives the ratio of the dynamic coefficient to its Taylor value $c^{dyn}_{k,n}/c^*_{k,n}$ as function of time. Clearly there is a sharp increase of this ratio around $t \approx 1$ where the shock is forming and the simulation shifts from DNS-resolution to LES-resolution. The results of the nonlinear scheme with $k = 2$ display a more inconsistent and irregular behavior. Although the nonlinear scheme is expected to obtain similar performance as the 4th-order tridiagonal DRP Padé scheme, its accuracy is only comparable at early times in the simulation. Once the spectrum is fully developed, the quality of the nonlinear scheme seems to be lost partially since it cannot meet the accuracy of the 4th-order tridiagonal Padé scheme. This suggests that the performance is neutralized due to nonlinear pollution in the scheme. Indeed, looking at the snapshots in Fig. 11 it can be observed that although at $t = 0.5$ the accuracy of the lower wavenumber modes lies between that of the 4th- and 6th- order central scheme, the error does not fade out for the higher wavenumber range as for the linear schemes. This clearly shows that the nonlinear dynamic scheme produces spurious scales with low energy, due to the nonlinear interactions in the scheme. These scales are distributed over the entire wavenumber range and affect the quality of every mode. At $t = 1.8$, the accuracy decreases to that of the 2nd-order scheme for the small wavenumber region, while spurious energy is created again in the entire wavenumber range even beyond the filter-cutoff. Although the nonlinear scheme seems to have better performance than its linear variant, it never reaches the accuracy of the 4th-order DRP Padé scheme. These findings suggests that the nonlinearity may impose an obstruction in order to safely apply this scheme for LES. This is further discussed in the a posteriori studies.

7.3. A posteriori results

7.3.1. Perfect subgrid-scale model

The results obtained from the large-eddy simulation of the Burgers' equation using the perfect subgrid-scale model are expected to be similar to those of the a priori study, since the LES-solution should approximately return the filtered DNS-solution. Hence, modeling errors are almost absent, and verification of this indeed shows a maximum modeling error on the kinetic energy of $\Delta k_{u,model} \approx 1 \cdot 10^{-7}$. Numerical errors are thus dominant for these simulations. However, in contrast to the a priori study, the finite difference discretization can now affect the solution as it evolves in time.

Fig. 13 shows the global magnitude of the numerical error as function of time. This error corresponds to the L_2-norm which is a mathematics-based error quantity, reflecting the error contributions on both amplitude and phase of the solution. The results look very similar to those of the a priori study. In the early stages of the simulation, the accuracy of the linear dynamic schemes with $k = 2$ and $k = 4$ again closely approach that of the standard 2nd-, respectively, 4th-order schemes, while the corresponding DRP schemes are less accurate. Once the shock is fully developed ($1 \leqslant t \leqslant 3$) the linear dynamic schemes and the corresponding DRP schemes display similar behavior. The linear dynamic scheme with $k = 2$ and the 2nd-order DRP scheme both obtain better accuracy than the 6th-order central scheme, while the 4th-order DRP scheme and the linear dynamic scheme with $k = 4$ even outperform the 6th-order Padé scheme. As the shock wave decays further e.g. at times $t \geqslant 3$, it can be seen that the DRP schemes lose their accuracy much faster than the linear dynamic schemes, and their errors become rapidly larger than those of the linear dynamic schemes. This again emphasizes the benefit of the adap-

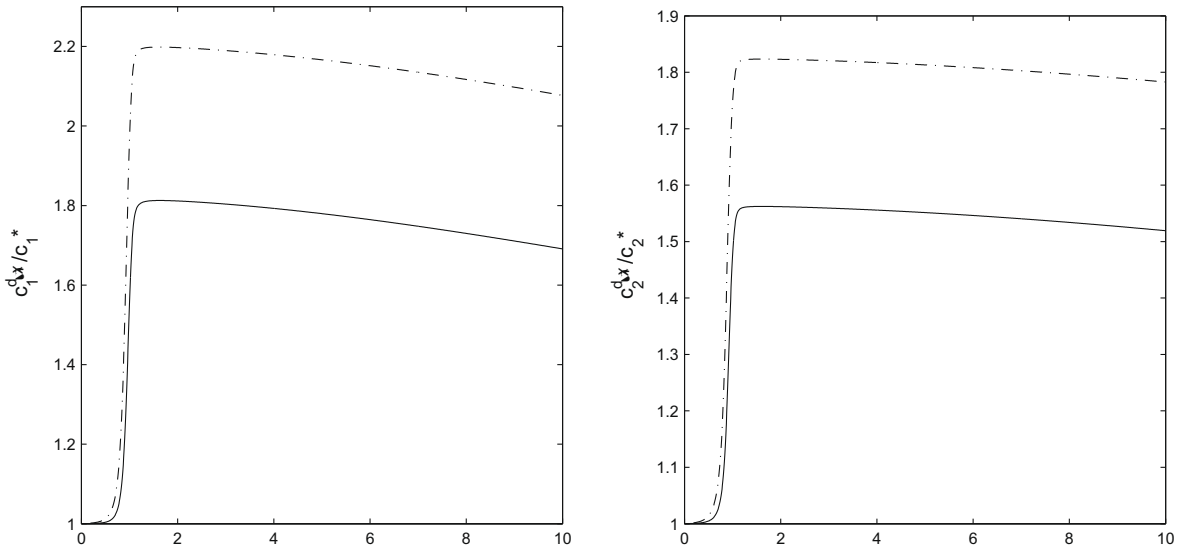

Fig. 12. *A priori results:* ratio of the dynamic coefficient $c^{dyn}_{k,n}/c^*_{k,n} = c^{dyn}_n/c^*_n$ to its Taylor value for the linear dynamic scheme with $k = 2$ (—) and $k = 4$ (–·–·). *Left:* $c^{dyn}_1/c^*_1(t)$ of the first derivative; *right:* $c^{dyn}_2/c^*_2(t)$ of the second derivative.

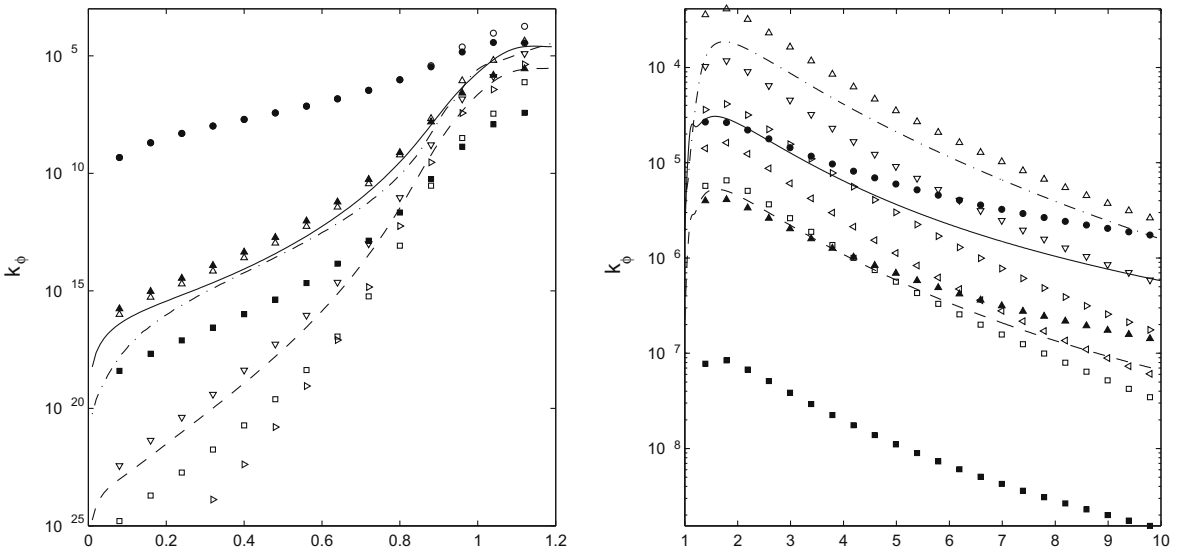

Fig. 13. *Perfect SGS model:* global magnitude k_ϕ of the error $\phi = \varepsilon_u$ before shock formation at $0 \leqslant t \leqslant 1.2$ (*left*) and after shock formation and decay at $1 \leqslant t \leqslant 10$ (*right*). (Symbols see Table 3.)

tive behavior of the dynamic schemes obtaining minimal errors according to the spectral properties of the flow field. For $t \to \infty$ the dynamic schemes should reduce again to their asymptotic equivalents. Fig. 14 displays two snapshots of the energy spectrum of the numerical error $E_\phi(\kappa, t), \phi = \varepsilon_u$ at times $t = 0.5$ and $t = 1.8$, which reflect the adaptable Fourier characteristics of the linear dynamic schemes. The numerical error on the energy spectrum $\varepsilon_E = \Delta E_u(\kappa, t)$ gives qualitatively similar results and is therefore not shown.

Looking at the performance of the nonlinear scheme ($k = 2$) results are much worse than in the a priori study. The accuracy remains generally around that of the 4th-order scheme although for the very early stages of the simulation ($t \leqslant 0.04$) it decreases to the level of the 4th-order DRP Padé scheme. It is obvious from Fig. 14 that the nonlinear interactions of the scheme severely pollute the solution e.g. at $t = 1.8$. Apparently, even the largest scales are significantly affected by the nonlinearity.

We proceed now by discussing the physics-based errors from Fig. 15 showing the numerical errors on the kinetic energy and dissipation rate. These physics-based errors mainly reflect differences in amplitude of the solution. The observations and conclusions from Fig. 13 mainly apply to the results of Fig. 15. Both linear dynamic schemes ($k = 2, 4$) perform very well as

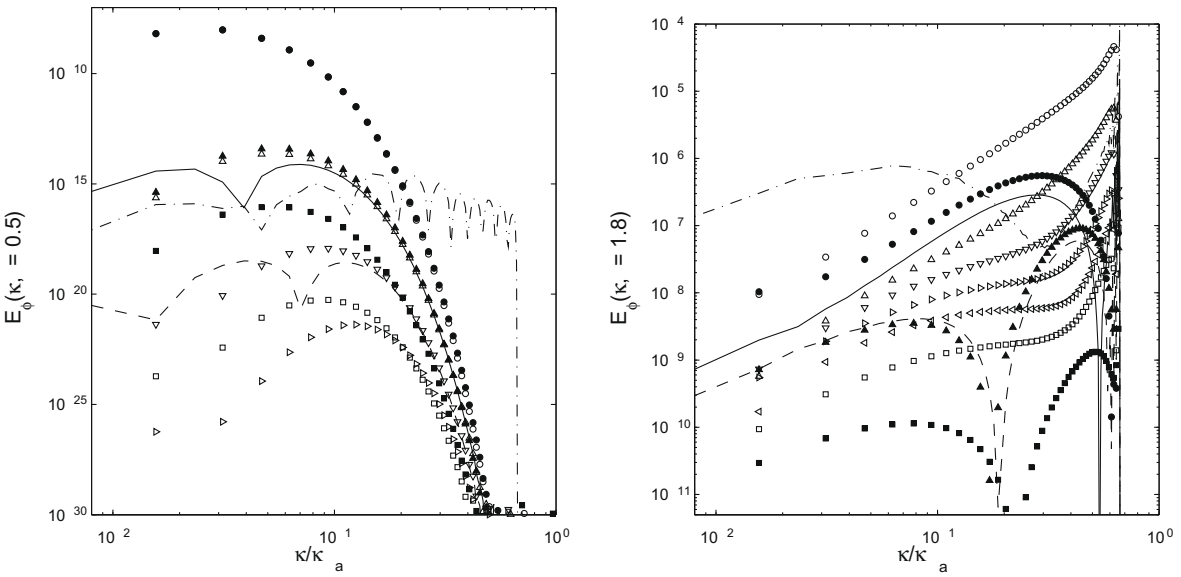

Fig. 14. *Perfect SGS model:* snapshots of the energy spectrum $E_\phi(\kappa, t)$ of the error $\phi = \varepsilon_u$ at times $t = 0.5$ (developing spectrum) (*left*) and $t = 1.8$ (fully developed spectrum) (*right*). (Symbols see Table 3.)

they converge to the asymptotic standard schemes for smooth velocity fields with low spectral content at the beginning of the simulations, while they adapt toward DRP-behavior when the shock is formed and a full inertial range of scales is present. Remarkably, the linear dynamic schemes with $k = 2, 4$ obtain much better accuracy in comparison to the equivalent 2nd- and 4th-order DRP schemes. This can be understood from the optimization procedure in Section 5.3, where the Burgers' spectrum is used to obtain the optimal value of the blending factor f_{opt}, instead of the uniform spectrum. On the other hand, the nonlinear scheme with $k = 2$ again leads to very poor accuracy improvement, as consequence of the nonlinear pollution.

Summarizing, the results of the linear dynamic schemes agree very well with the performance expected from the theoretical analysis. The encouraging results seem to support the hypothesis that such dynamically optimized schemes may provide an advantageous tool for numerically accurate large-eddy simulations. Further we have seen that nonlinear schemes are not appropriate for the purpose of accurate flow simulations, since spurious wavenumber modes are produced due to nonlinear interactions in the scheme. These spurious scales strongly affect the solution.

7.3.2. Dynamic Smagorinsky model

Finally, we investigate the performance of the dynamic schemes in the large-eddy simulation of the Burgers' equation using a dynamic Smagorinsky model. In contrast to the perfect subgrid-sca[illegible]ow significant modeling errors arise,

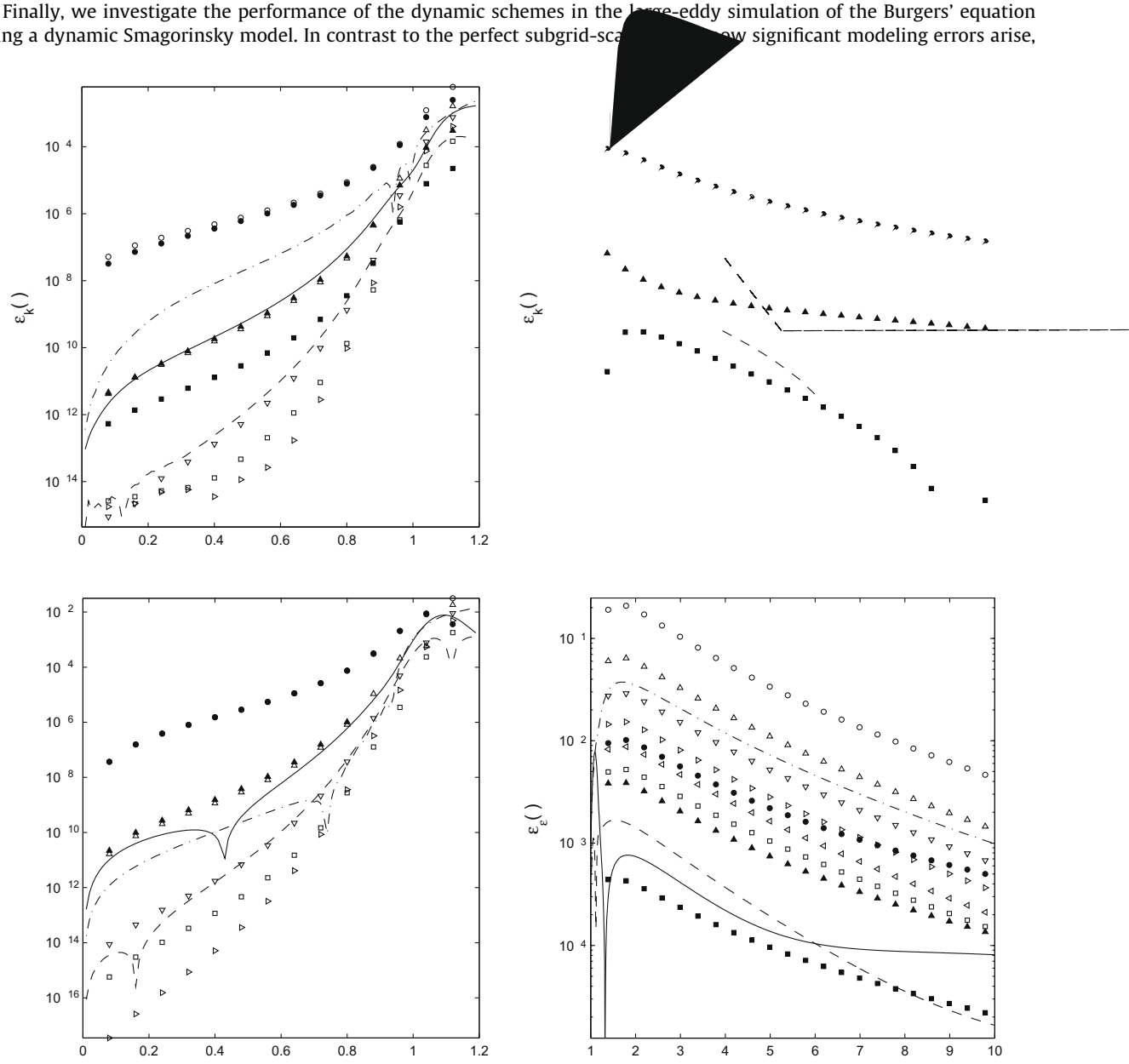

Fig. 15. *Perfect SGS model:* error on the kinetic energy $\varepsilon_k = \Delta k_u$ (*upper*) and error on the dissipation rate $\varepsilon_\varepsilon = \Delta\varepsilon$ (*lower*) before shock formation at $0 \leqslant t \leqslant 1.2$ (*left*) and after shock formation and decay at $1 \leqslant t \leqslant 10$ (*right*). (Symbols see Table 3.)

which interact with the numerical errors and vice versa, making the results somehow unpredictable. Therefore, we try to visualize these interactions by separating modeling errors and numerical errors. The exact modeling error on the kinetic energy and the dissipation rate are shown in Fig. 16. The positive modeling error, indicates that the dynamic Smagorinsky model is slightly too dissipative, since the kinetic energy of the spectral LES is smaller than the DNS. It was further verified from the detailed results that the subgrid model is especially too dissipative for the large and medium scales, whereas an energy pile-up occurs near the filter cutoff. The pile-up is due to the inability of the eddy viscosity model to describe well the cusped behavior of the spectral viscosity at the sharp cutoff. Nevertheless, the general performance of the dynamic Smagorinsky model appears satisfactory since the κ^{-2} inertial range is approximated fairly good. Fig. 16 shows also the dynamic model coefficient $C_{s,s}^2$ of the pseudo-spectral LES together with the turbulent viscosity. As expected, the dynamic procedure engages the model at $t \approx 1$ and automatically finds the quasi-optimal value as the shock decays. Note that the value of the dynamic coefficient is higher for Burgers' turbulence than for Kolmogorov turbulence, due to the essential differences in the dynamics of the small scales.

In Figs. 17 and 18 the mathematics-based errors are presented. Fig. 17 gives a measure for the L_2-norm as function of time, whereas Fig. 18 displays the energy spectrum of the numerical errors at $t = 0.5$ and $t = 1.8$. Generally the same conclusion can be drawn for the linear dynamic schemes with $k = 2, 4$ and the corresponding DRP schemes, as in case of the perfect subgrid scale model. The linear dynamic schemes obtain asymptotic accuracy for the early stages, in contrast to the DRP schemes, and they adapt to the flow physics as the simulation proceeds, leading to equivalent accuracy as the DRP schemes which is much better than that of the standard central schemes. The linear dynamic scheme with $k = 2$ reaches accuracy better then the 8th-order central scheme, while the linear dynamic scheme with $k = 4$ reaches almost the quality of the 6th-order standard Padé scheme. Although the nonlinear dynamic scheme with $k = 2$ still produces spurious small scales which inevitable interact with all scales of motion, it performs surprisingly better in combination with the dynamic Smagorinsky model instead of the perfect subgrid-scale model. Albeit the reasons for this behavior remain somewhat unclear, we assume that the creation of spurious scales compensates the over-dissipative nature of the Smagorinsky model, resulting in a better overall behavior. Despite this unforeseen advantage, application of the nonlinear scheme remains questionable for LES.

Fig. 19 shows the physics-based errors on the velocity field, i.e the absolute value of the error on the kinetic energy and on the dissipation rate. Results are analogous to the ones previously discussed, displaying the very good behavior of the linear dynamic schemes, and the unexpected good behavior of the nonlinear scheme. Nevertheless, some remarkable results are obtained. Looking at the error on the kinetic energy ε_k in Fig. 19, especially the linear dynamic scheme with $k = 2$ performs very well as it reaches almost the quality of the 6th-order standard Padé scheme. However, this is not observed for the error on the dissipation rate in Fig. 19 where the linear dynamic scheme with $k = 2$ reaches approximately 8th-order accuracy. The error on the dissipation rate focusses more on the accuracy of the small scales than does the error on the kinetic energy. This emphasizes the importance of looking at different error measures, since they indicate different phenomena, confirming the studies in [32,5].

We proceed our investigation of numerical errors by examining the influence of the numerics on the dynamic procedure itself. Fig. 20 gives the relative error-percentages between the model coefficients $C_{s,fd}$ of the finite difference simulations and

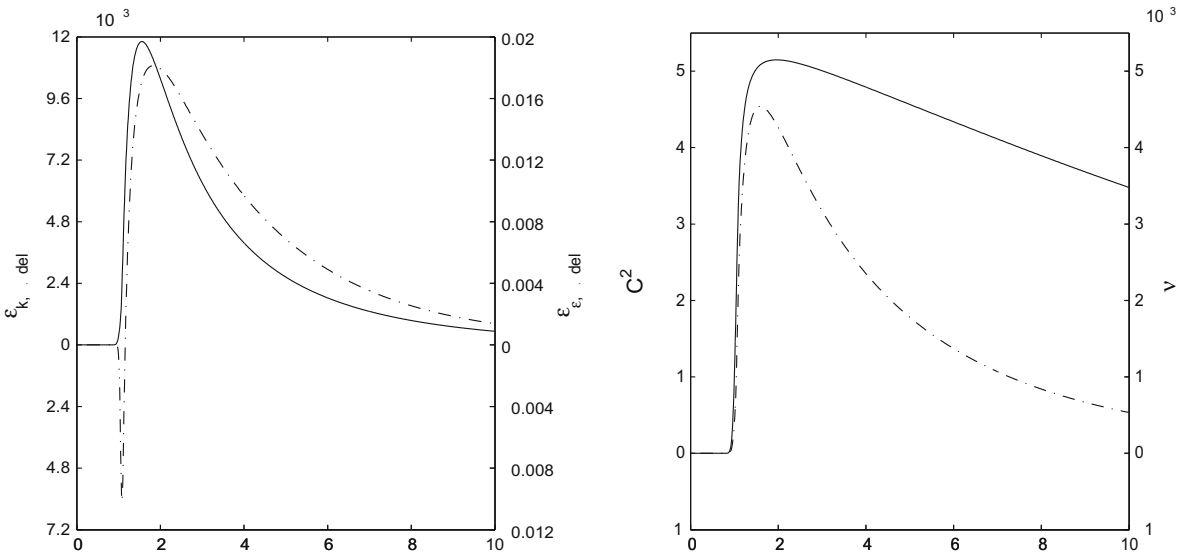

Fig. 16. *Dynamic SGS model:* modeling errors on kinetic energy k_u (—) and dissipation ϵ (– · – ·) (*left*). Dynamic Smagorinsky constant $C_{s,s}^2$ (—) and the turbulent viscosity ν_t (– · – ·) from the pseudo-spectral LES *right*.

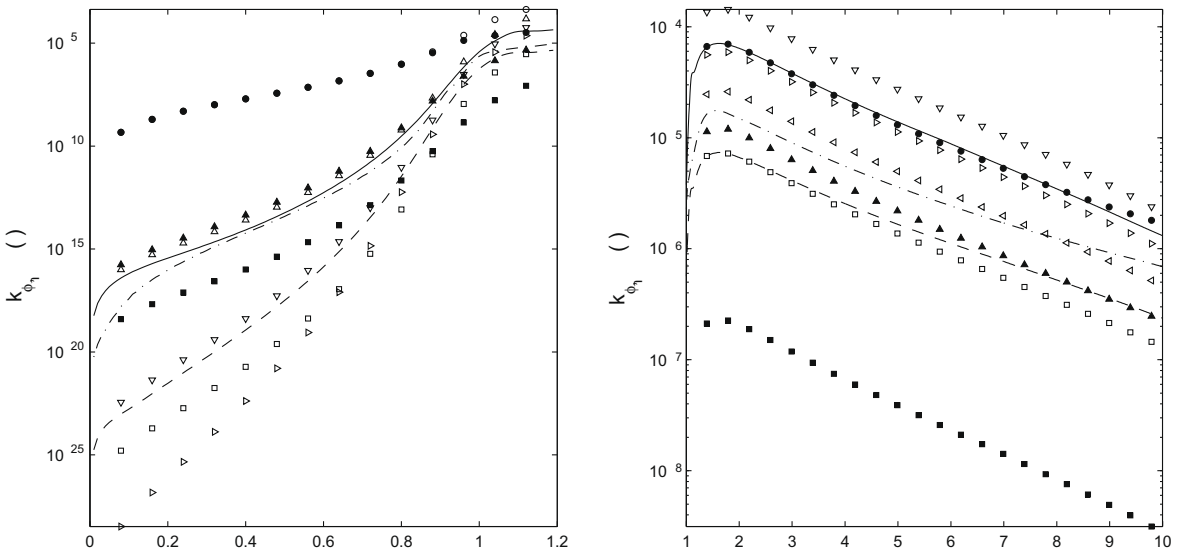

Fig. 17. *Dynamic SGS model:* global magnitude k_ϕ of the error $\phi = \varepsilon_u$ before shock formation at $0 \leqslant t \leqslant 1.2$ (*left*) and after shock formation and decay at $1 \leqslant t \leqslant 10$ (*right*). (Symbols see Table 3.)

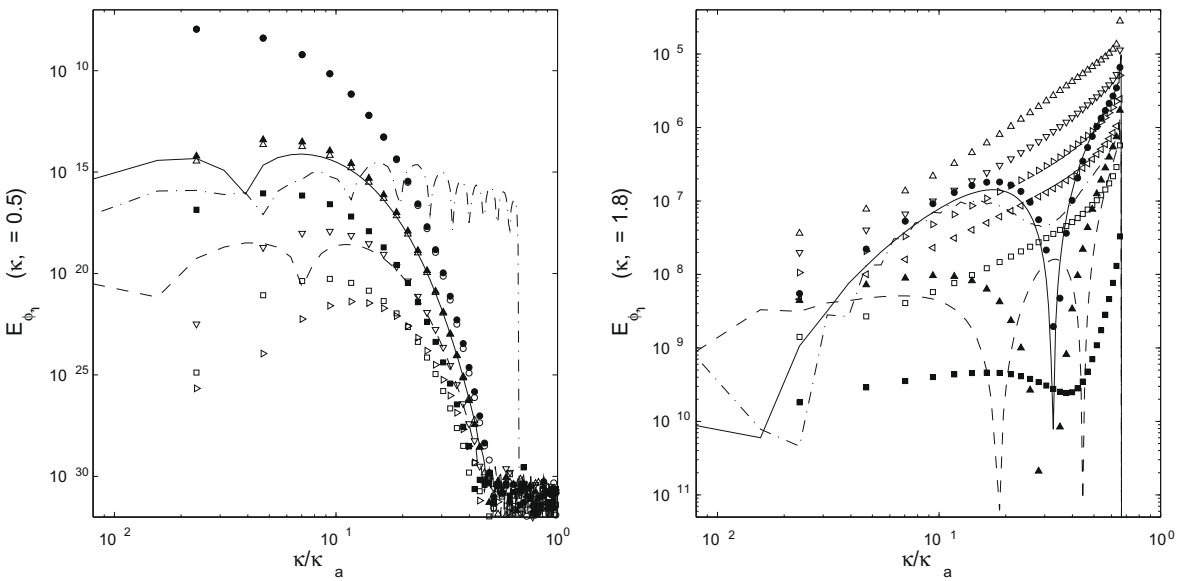

Fig. 18. *Dynamic SGS model:* snapshots of the energy spectrum $E_\phi(\kappa, t)$ of the error $\phi = \varepsilon_u$ at times $t = 0.5$ (developing spectrum) (*left*) and $t = 1.8$ (fully developed spectrum) (*right*). (Symbols see Table 3.)

the $C_{s,s}$ of the pseudo-spectral simulation, and the deviation between $C_{s,fd}$ and $C_{fd,fd}$ of the finite difference simulations. These relative errors are defined by

$$\Delta C_s^2 = \frac{C_{s,s}^2 - C_{s,fd}^2}{C_{s,s}^2}, \tag{63}$$

$$\Delta C_{fd}^2 = \frac{C_{s,fd}^2 - C_{fd,fd}^2}{C_{s,fd}^2}. \tag{64}$$

First, the model coefficient $C_{s,fd}$ is systematically larger for low order schemes than for high-order schemes compared to its *theoretical* value $C_{s,s}$. This may be explained by the fact that the dynamic procedure tries to compensate for the reduced effectiveness of the subgrid dissipation on the smallest resolved scales when using low order schemes. Hence, the dynamic Ger-

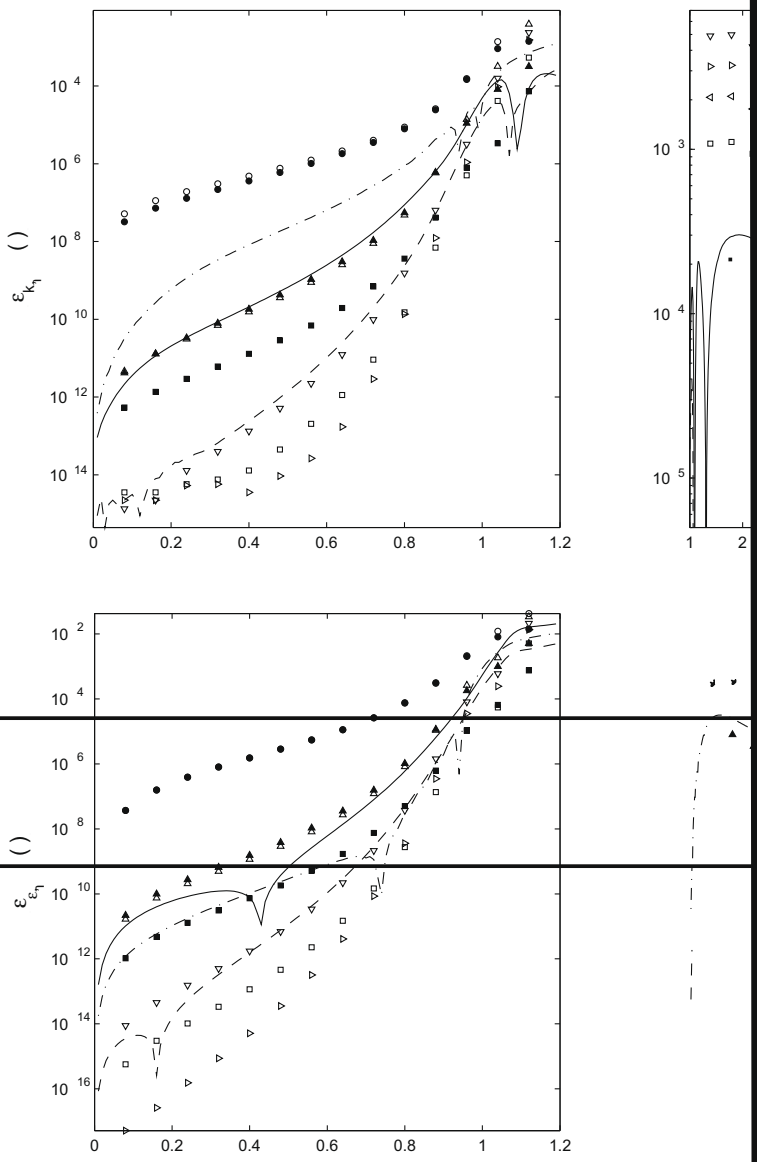

mano procedure responds to numerical shortcomings of the low-order finite di
This results into a larger subgrid dissipation on the small scales, which are s
unfortunately also on the large scales, which are much less affected by the r
of Meyers et al. [33]. Secondly, the influence of discretization errors on the gra
in a systematical underestimation of the dynamic model coefficient $C_{fd,fd}$ in co
that the 2nd-order central scheme has the most severe underestimation of $C_{fd,}$
coefficient is the largest, it tends to overestimate $C_{fd,fd}$ toward the end of the
higher-order schemes, and one may conclude that increase of $C_{s,fd}$ compared to
tions, is partially compensated by the decrease of $C_{fd,fd}$ in comparison with $C_{s,f}$
procedure itself. Finally, it was verified that the coefficient $C_{fd,fd}$ is smaller tha
sipation is reduced, resulting in higher levels of kinetic energy in the LES-simu
the Smagorinsky model is seen to be too dissipative in the mean. In conclusion
mum between dissipation on the large scales and that on the small scales. Ve
the dynamic Smagorinsky model, the dissipation on the large scales is too hig

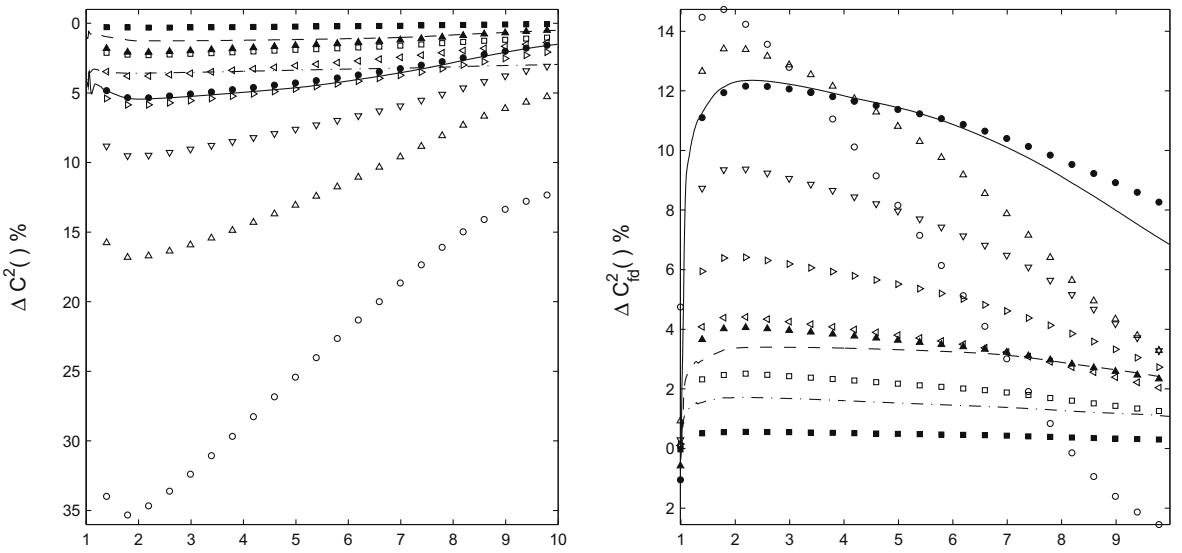

Fig. 20. *Dynamic SGS model:* relative error of $C_{s,fd}$ compared to $C_{fd,fd}$ (*left*): influence of discretization errors on the value of the dynamic constant. Relative error of $C_{fd,fd}$ compared to $C_{s,fd}$ (*right*): influence of discretization errors in the Germano procedure on the calculation of the dynamic constant. (Symbols see Table 3.)

leading to a pile-up near the cutoff. It may be obvious that a hyper-viscosity model combined with a dynamic procedure would probably lead to less dissipation on the large scales and better dissipation on the small scales.

It may be clear by now that numerics and modeling are completely entwined in large-eddy simulations, especially when using more advanced subgrid models such as the dynamic model. In the previous discussion the influence of the interactions between numerics and modeling on the level of the model constant was shown. Although this gave more insight in how the dynamic Smagorinsky model acts, it does not indicate whether a better approximation of the model will lead to a better overall performance. Therefore, we further compare the finite difference LES-solutions with those of the filtered DNS. Comparison of the results with the filtered DNS, implies that the total error $\varepsilon_{u,total}$, which includes numerical and modeling errors, is taken into account, whereas comparison with the spectral LES results, implies that only the numerical error $\varepsilon_{u,num}$ is taken into account. Fig. 21 gives the error between the energy spectra at $t = 1.8$ of the finite difference LES-solutions on the one hand, and the filtered DNS-solution or the pseudo-spectral LES-solution on the other hand.

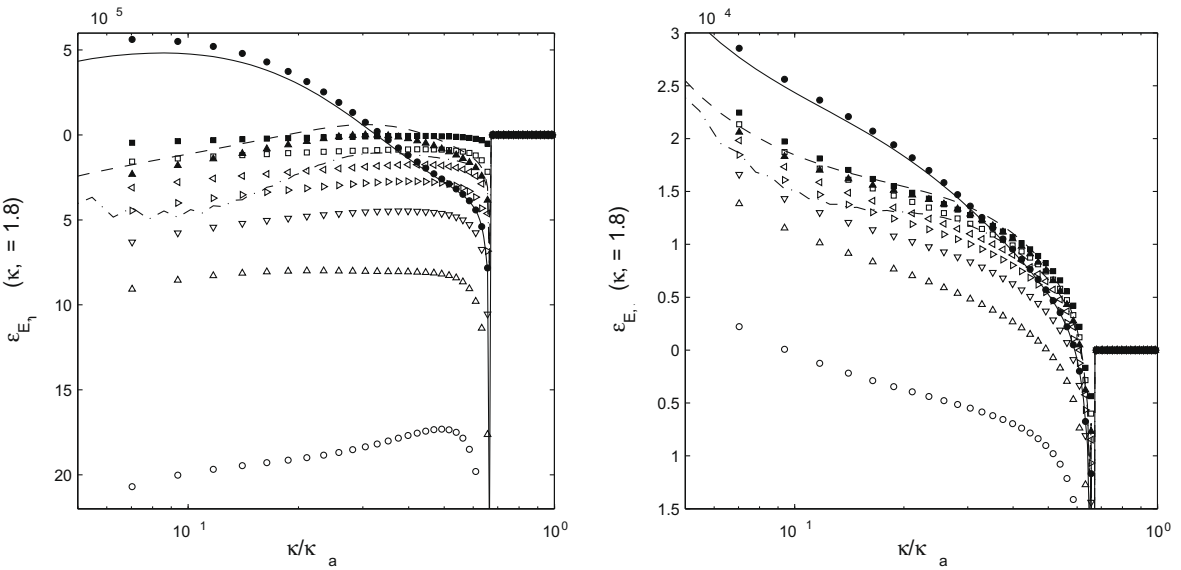

Fig. 21. *Dynamic SGS model:* numerical error and total error on the energy spectrum $\Delta E_u(\kappa, t)$ of the velocity field at time $t = 1.8$: numerical error (*left*); total error (numerical + modeling) (*right*). (Symbols see Table 3.)

In accordance with the results of the perfect subgrid-scale model, the full numerical discretization error decreases with increasing accuracy of the numerical schemes. However, almost the opposite is observed when looking at the total error, i.e. the difference between the filtered DNS-solution and the finite difference LES-solution. There, the 2nd-order finite difference LES leads to the lowest errors on the largest scales, whereas the higher-order methods appear to perform better on the smallest resolved scales. It was verified from the results, that eventually the 4th-order finite difference solution leads to the lowest errors on the kinetic energy, whereas the more accurate schemes lead to the lowest errors on the dissipation rate. This proves that partial cancellation between the numerical errors and modeling errors can occur as shown by Meyers et al. [20], but that it strongly depends on the error measure used in the error evaluation.

8. Computational cost and robustness

Although the results are excellent, the *current implementation* of the method requires the calculation of approximately three dynamic coefficients, leading inevitably to a significant computational overhead. It was found for the large-eddy simulation of the Burgers' equation, that the *total computational time* was about 20% higher for the dynamic schemes compared to the DRP schemes, which may be considered prohibitive for practical computations. Nevertheless, this premature conclusion must be placed in perspective. In the current work, the dynamic finite difference schemes were implemented straightforwardly and rigorously. This implies that each of the three dynamic coefficients was calculated at each Runge–Kutta stage, that is four times per time step. However, it might be sufficient to calculate each dynamic coefficient only once per time step, or even once per few time steps, depending on the time increment Δt. Indeed, since the time scale ratio $\theta = \Delta t/\tau_\eta$ must be chosen sufficiently small in order to avoid numerical dissipation, one cannot expect the physics to change much during one time step. Hence, evaluating the coefficients each θ timesteps might be sufficient. This strategy is illustrated hereafter.

Consider the variable θ_s, which indicates the required CPU-time per Runge–Kutta step for a large-eddy simulation, using a finite difference method with *static* predefined stencil coefficients. Similarly consider the variable θ_d, which indicates the required CPU-time per Runge–Kutta step for a large-eddy simulation using a finite difference method with *dynamic*, real-time calculated stencil coefficients. Then, $\Delta\theta = \theta_d - \theta_s$ gives the computational overhead for the calculation of the dynamic coefficients per Runge–Kutta step. Further, assume a q-stage Runge–Kutta method for the time-integration of the large-eddy simulation over N_t time steps. The computational CPU-time per Runge–Kutta step θ_d can now be expressed as function of θ_s, i.e.

$$\theta_d = \theta_s + \Delta\theta \frac{q'}{q} \frac{N_t'}{N_t}, \tag{65}$$

where the ratio q'/q determines the number of evaluations per q stages and N_t'/N_t determines the total number of evaluations per N_t time steps. Fig. 22 illustrates the reduction of the computational overhead for the large-eddy simulation of Burgers' equation in the current work, where $q = 4$ and $N_t = 1 \cdot 10^{-6}$.

For example, if all dynamic coefficients are evaluated only once every time step, i.e. $q'/q = 1/4$ and $N_t'/N_t = 1$, the computational overhead is only 5%, which is a substantial reduction compared to the original 20%. If all dynamic coefficients are only evaluated every $\theta = 10$ time steps ($q'/q = 1/4$ and $N_t'/N_t = 1/10$), the overhead is only 0.5%, which is negligible. Obvi-

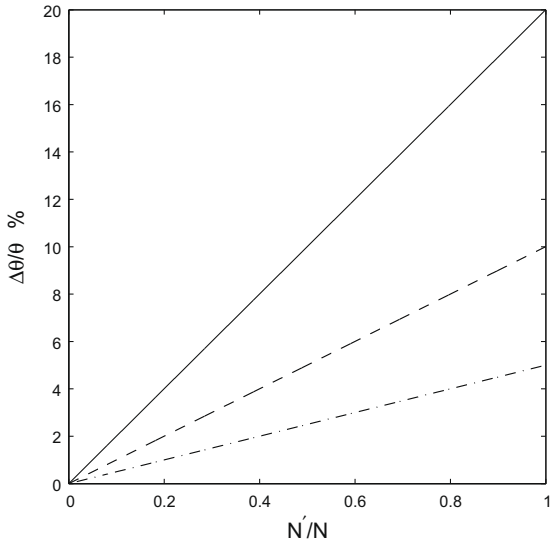

Fig. 22. *Computational overhead.* Reduction of the computational overhead as function of N_t'/N_t for $q'/q = 1$ (—), $q'/q = 1/2$ (– – –) and $q'/q = 1/4$ (– · – ·).

ously, such strategies make the dynamic schemes relatively cheap compared to its quality, which makes them competitive with the dispersion-relation preserving schemes. Such strategies will be investigated in more detail in future work.

Finally, we comment about the robustness of the developed dynamic finite difference schemes in the present work. As mentioned before, The coefficient of the nonlinear dynamic schemes was restricted according to the theoretical extrema of expression (32), in order to avoid accidental singularities. On the other hand, the linear dynamic schemes are sufficiently robust since no clippings on the constant dynamic coefficients were needed in this work in order to guarantee the stability. However, a particularity arises if the velocity field is constant, i.e. if $\kappa/\kappa_{max} \equiv 0$. Indeed, according to relations (18) and (28), the dynamic coefficient is indefinite, i.e. $c_{k,n}^{dyn} = 0/0$, in such cases. This particularity can easily be excluded, by enforcing $c_{k,n}^{dyn} = 0$ and is justified since any finite difference scheme returns the exact value for the derivative of a constant field.

9. Conclusions and future work

In this work, a family of *dynamic* finite difference schemes were presented as a tool for accurate large-eddy simulation. More specifically, two linear and one nonlinear variant were discussed. The emphasis of these schemes is on optimal representation of Fourier modes within the wavenumber range $\kappa \in [0, 2\pi/3\Delta]$, rather than obtaining asymptotic accuracy for the lowest wavenumber modes. Although the constructed dynamic schemes share similarities with the dispersion-relation preserving schemes of Tam and Webb [7], their behavior is more refined. The presented schemes are dynamically adapted during the simulation through a dynamic coefficient $c_{k,n}^{dyn}$ which is calculated from the flow field. Hence, the corresponding Fourier characteristics vary in time according to the flow physics such that the global dispersion error is minimized. This is in contrast to prefactored dispersion-relation preserving schemes, which have predefined Fourier characteristics. Only the sensitivity of the schemes to high-wavenumber modes in the generic turbulent spectrum is set a priori by an additional parameter, which is considered generally applicable for a wide range of turbulent flows. The dynamic behavior, and the resulting high numerical quality has been extensively investigated both analytically and numerically by large-eddy simulation of Burgers' equation with different subgrid models. Several specific conclusions can be drawn for both the linear dynamic scheme and the nonlinear dynamic scheme.

(i) For velocity fields that are well resolved on the computational grid such that they show a smooth behavior on the grid scale e.g. in laminar flows or in case of DNS-resolution, the linear dynamic schemes tend toward the corresponding asymptotic high-order standard central schemes, focusing on maximum accuracy for the largest scales. This is an advantage over the DRP schemes which remain suboptimal for those flows, since they are designed a priori assuming a uniform spectrum in the region $\kappa \in [0, 2\pi/3\Delta]$.

(ii) During transitional stages, when the highest wavenumber modes of the developing energy spectrum gain in energy, the linear dynamic schemes seamlessly optimize themselves according to the changing spectral content. The sensitivity with which the scheme adapts to high-wavenumber modes in the energy spectrum is predefined by the blending factor f.

(iii) Once the flow is fully developed, exhibiting full inertial range behavior, the linear dynamic scheme acts like a DRP scheme, minimizing the dispersion errors for all scales in the wavenumber range $\kappa \in [0, 2\pi/3\Delta]$.

(iv) The nonlinear dynamic scheme, which contains a pointwise varying dynamic coefficient, should exhibit similar performance as the tridiagonal DRP Padé scheme according to analytical analysis. However, due to nonlinearity, spurious scales are produced in the range $\kappa \in [0, \pi/\Delta]$, severely polluting the solution and substantially reducing accuracy of the Burgers' solution. Therefore, the nonlinear dynamic scheme may not be appropriate for large-eddy simulations of realistic turbulent flows, as it produces spurious energy. This conclusion may be extrapolated toward all nonlinear schemes.

(v) The schemes have been tested in an a priori and an a posteriori study of LES of the viscous Burgers' equation, in which a sine wave develops toward a shock wave. Moreover, two subgrid models are applied: the perfect subgrid model and the dynamic Smagorinsky model. The results showed a significant increase in numerical accuracy, confirming the large potential of this methodology. Although the dynamic schemes involve an additional cost due to the calculation of the dynamic coefficient at each iteration, it was argued that it may sufficient to determine these coefficients only every few time steps. Such a strategy, would lead to a negligible computational overhead.

(vi) Finally, despite the large numerical accuracy improvement of the high-order schemes, it was shown that low-order methods may have advantageous cancellation between numerical errors and modeling errors resulting in a reduction of the total errors on some quantities. However, the opposite was observed for quantities that accentuate the small scales. Although it is tempting to resign to application of lower-order discretizations in combination with dissipative models, trusting upon contingent cancellation of errors, we advocate to develop better models in combination with highly accurate discretizations such that both numerical errors and modeling errors are controlled more systematically.

Although we illustrated the performance of the developed dynamic finite difference schemes only for large-eddy simulation of Burgers' turbulence in this work, we already successfully applied these schemes to the large-eddy simulation of three-dimensional transitional Taylor–Green vortex flow. The results of this study will be reported in future work together with the general construction of dynamic compact Padé schemes.

Acknowledgment

This research was funded by a Ph.D. grant of the Institute for the Promotion of Innovation through Science and Technology in Flanders (IWT-Vlaanderen).

Appendix A. Dynamic finite difference approximations

A.1. Order of accuracy $k = 2$

A.1.1. First derivative ($n = 1$)

The basic expression for the dynamic finite difference approximation of the first derivative in a node $\bar{u}(x_i) = \bar{u}_i$ is given by

$$\overline{\frac{\partial u}{\partial x}}(x) = \frac{\delta \bar{u}}{\delta x} + c_1^{dyn} \Delta^2 \frac{\delta^3 \bar{u}}{\delta x^3}, \tag{A.1}$$

in which c_1^{dyn} is calculated with expression (18). From Taylor expansion we obtain the values $c_1^* = -1/6$ and $c_1^{**} = -1/4$, while the finite difference approximations of the derivatives are given by

$$\frac{\delta \bar{u}}{\delta x} = \frac{-\bar{u}_{i-1} + \bar{u}_{i+1}}{2\Delta}, \tag{A.2}$$

$$\frac{\delta^3 \bar{u}}{\delta x^3} = \frac{-\bar{u}_{i-2} + 2\bar{u}_{i-1} - 2\bar{u}_{i+1} + \bar{u}_{i+2}}{2\Delta^3}, \tag{A.3}$$

$$\frac{\delta^5 \bar{u}}{\delta x^5} = \frac{-\bar{u}_{i-3} + 4\bar{u}_{i-2} - 5\bar{u}_{i-1} + 5\bar{u}_{i+1} - 4\bar{u}_{i+2} + \bar{u}_{i+3}}{2\Delta^5}. \tag{A.4}$$

A.1.2. Second derivative ($n = 2$)

The basic expression for the dynamic finite difference approximation of the second derivative in a node $\bar{u}(x_i) = \bar{u}_i$ is given by

$$\overline{\frac{\partial^2 u}{\partial x^2}}(x) = \frac{\delta^2 \bar{u}}{\delta x^2} + c_2^{dyn} \Delta^2 \frac{\delta^4 \bar{u}}{\delta x^4}, \tag{A.5}$$

in which c_2^{dyn} is calculated with expression (18). From Taylor expansion we obtain the values $c_1^* = -1/12$ and $c_2^{**} = -1/6$, while the finite difference approximations of the derivatives are given by

$$\frac{\delta^2 \bar{u}}{\delta x^2} = \frac{\bar{u}_{i-1} - 2\bar{u}_i + \bar{u}_{i+1}}{\Delta^2}, \tag{A.6}$$

$$\frac{\delta^4 \bar{u}}{\delta x^4} = \frac{\bar{u}_{i-2} - 4\bar{u}_{i-1} + 6\bar{u}_i - 4\bar{u}_{i+1} + \bar{u}_{i+2}}{\Delta^4}, \tag{A.7}$$

$$\frac{\delta^6 \bar{u}}{\delta x^6} = \frac{\bar{u}_{i-3} - 6\bar{u}_{i-2} + 15\bar{u}_{i-1} - 20\bar{u}_i + 15\bar{u}_{i+1} - 6\bar{u}_{i+2} + \bar{u}_{i+3}}{\Delta^6}. \tag{A.8}$$

A.2. Order of accuracy $k = 4$

A.2.1. First derivative ($n = 1$)

The basic expression for the dynamic finite difference approximation of the first derivative in a node $\bar{u}(x_i) = \bar{u}_i$ is given by

$$\overline{\frac{\partial u}{\partial x}}(x) = \frac{\delta \bar{u}}{\delta x} + c_1^{dyn} \Delta^4 \frac{\delta^5 \bar{u}}{\delta x^5}, \tag{A.9}$$

in which c_1^{dyn} is calculated with expression (18). From Taylor expansion we obtain the values $c_1^* = 1/30$ and $c_1^{**} = -1/3$, while the finite difference approximations of the derivatives are given by

$$\frac{\delta \bar{u}}{\delta x} = \frac{\bar{u}_{i-2} - 8\bar{u}_{i-1} + 8\bar{u}_{i+1} - \bar{u}_{i+2}}{12\Delta}, \tag{A.10}$$

$$\frac{\delta^5 \bar{u}}{\delta x^5} = \frac{-\bar{u}_{i-3} + 4\bar{u}_{i-2} - 5\bar{u}_{i-1} + 5\bar{u}_{i+1} - 4\bar{u}_{i+2} + \bar{u}_{i+3}}{2\Delta^5}, \tag{A.11}$$

$$\frac{\delta^7 \bar{u}}{\delta x^7} = \frac{-\bar{u}_{i-4} + 6\bar{u}_{i-3} - 14\bar{u}_{i-2} + 14\bar{u}_{i-1} - 14\bar{u}_{i+1} + 14\bar{u}_{i+2} - 6\bar{u}_{i+3} + \bar{u}_{i+4}}{2\Delta^7}. \tag{A.12}$$

A.2.2. Second derivative ($n = 2$)

The basic expression for the dynamic finite difference approximation of the second derivative in a node $\bar{u}(x_i) = \bar{u}_i$ is given by

$$\overline{\frac{\partial^2 u}{\partial x^2}}(x) = \frac{\delta^2 \bar{u}}{\delta x^2} + c_2^{dyn} \Delta^4 \frac{\delta^6 \bar{u}}{\delta x^6}, \tag{A.13}$$

in which c_2^{dyn} is calculated with expression (18). From Taylor expansion we obtain the values $c_1^* = 1/90$ and $c_2^{**} = -1/4$, while the finite difference approximations of the derivatives are given by

$$\frac{\delta^2 \bar{u}}{\delta x^2} = \frac{-\bar{u}_{i-2} + 16\bar{u}_{i-1} - 30\bar{u}_i + 16\bar{u}_{i+1} - \bar{u}_{i+2}}{12\Delta^2}, \tag{A.14}$$

$$\frac{\delta^6 \bar{u}}{\delta x^6} = \frac{\bar{u}_{i-3} - 6\bar{u}_{i-2} + 15\bar{u}_{i-1} - 20\bar{u}_i + 15\bar{u}_{i+1} - 6\bar{u}_{i+2} + \bar{u}_{i+3}}{\Delta^6}, \tag{A.15}$$

$$\frac{\delta^8 \bar{u}}{\delta x^8} = \frac{\bar{u}_{i-4} - 8\bar{u}_{i-3} + 28\bar{u}_{i-2} - 56\bar{u}_{i-1} + 70\bar{u}_i - 56\bar{u}_{i+1} + 28\bar{u}_{i+2} - 8\bar{u}_{i+3} + \bar{u}_{i+4}}{\Delta^8}. \tag{A.16}$$

Appendix B. Conservative formulation

All linear finite difference schemes, including the linear dynamic scheme, are a priori conservative since they can be rewritten as the discrete divergence of a certain (higher-order) approximation of the velocity field. This approximation is then defined in finite difference context as

$$\overline{\frac{\partial^n u}{\partial x^n}}(x) = \frac{\delta^n \bar{u}_{approx}}{\delta x^n} = \frac{\delta^n}{\delta x^n}\left(\bar{u} + c_{k,n}\Delta^k \overline{\frac{\delta^k u}{\delta x^k}} + \mathcal{O}(\Delta^{k+2})\right), \tag{B.1}$$

in which the central discrete derivate $\delta^n/\delta x^n$ should have the minimal stencil width corresponding with the 2nd-order central approximation. $\bar{u}_{approx}$ is the higher-order reconstruction of the velocity field by Taylor series expansion. For the linear schemes, the divergence and non-divergence formulations are equal on a discrete level. However, it can be understood that the nonlinear scheme is not written in an a priori conservative formulation because the dynamic coefficient is pointwise varying. This can be remedied by taking the divergence of a low-dispersive dynamic reconstruction definition. Consider the general definition

$$\bar{u}_{approx}(x) = \bar{u} + c_{k,n}\Delta^k \overline{\frac{\delta^k u}{\delta x^k}} + \mathcal{O}(\Delta^k). \tag{B.2}$$

Following the same procedure as in Section 3, we can extract the nonlinear dynamic coefficient from this definition and obtain

$$c_{k,n}^{dyn} = -\frac{\mathcal{L}}{\mathcal{M}} = \frac{c_{k,n}^*}{1 - \dfrac{2^k(1-2^2)}{1-2^k}\Delta^2 f c_{k,n}^{**} \dfrac{\left.\overline{\dfrac{\delta^{k+2}\bar{u}}{\delta x^{k+2}}}\right|^{\Delta}}{\left.\overline{\dfrac{\delta^k \bar{u}}{\delta x^k}}\right|^{\Delta}}}. \tag{B.3}$$

Taking the divergence of this dynamic reconstruction series gives the conservative formulation of the nonlinear dynamic scheme. The constants $c_{k,n}^*$ and $c_{k,n}^{**}$ remain those of the non-conservative formulation. This way the modified wavenumbers of the conservative and non-conservative formulation are identical, and thus the expected accuracy should be preserved. Remark that calculation of the dynamic coefficient from the conservative formulation is advantageous, since the derivatives have more compact stencil widths, leading to less computational cost.

Appendix C. Modified wavenumbers

The modified wavenumbers for kth-order standard finite difference approximations of the 1^{st} derivative are

$$\kappa_1'(k=2) = \frac{\sin(\kappa\Delta)}{\Delta}, \tag{C.1}$$

$$\kappa_1'(k=4) = -\frac{\sin(2\kappa\Delta) - 8\sin(\kappa\Delta)}{6\Delta}, \tag{C.2}$$

$$\kappa_1'(k=6) = -\frac{-\sin(3\kappa\Delta) + 9\sin(2\kappa\Delta) - 45\sin(\kappa\Delta)}{30\Delta}, \tag{C.3}$$

$$\kappa_1'(k=8) = -\frac{3\sin(4\kappa\Delta) - 32\sin(3\kappa\Delta) + 168\sin(2\kappa\Delta) - 672\sin(\kappa\Delta)}{420\Delta}, \tag{C.4}$$

$$\kappa_1'(k=10) = -\frac{-2\sin(5\kappa\Delta) + 25\sin(4\kappa\Delta) - 150\sin(3\kappa\Delta) + 600\sin(2\kappa\Delta) - 2100\sin(\kappa\Delta)}{1260\Delta}. \tag{C.5}$$

The modified wavenumbers for kth-order standard finite difference approximations of the 1st derivative are

$$\kappa_2'^2(k=2) = \frac{2-2\cos(\kappa\Delta)}{\Delta^2}, \tag{C.6}$$

$$\kappa_2'^2(k=4) = \frac{\cos(2\kappa\Delta)-16\cos(\kappa\Delta)+15}{6\Delta^2} \tag{C.7}$$

$$\kappa_2'^2(k=6) = \frac{-2\cos(3\kappa\Delta)+27\cos(2\kappa\Delta)-270\cos(\kappa\Delta)+245}{90\Delta^2}, \tag{C.8}$$

$$\kappa_2'^2(k=8) = \frac{9\cos(4\kappa\Delta)-128\cos(3\kappa\Delta)+1008\cos(2\kappa\Delta)-8064\cos(\kappa\Delta)+7175}{2520\Delta^2}, \tag{C.9}$$

$$\kappa_2'^2(k=10) = \frac{-8\cos(5\kappa\Delta)+125\cos(4\kappa\Delta)-1000\cos(3\kappa\Delta)+6000\cos(2\kappa\Delta)-42000\cos(\kappa\Delta)+36883}{12600\Delta^2}. \tag{C.10}$$

The modified wavenumbers of higher derivatives for the 2nd-order standard finite difference approximation are

$$\kappa_3'^3 = \frac{-\sin(2\kappa\Delta)+2\sin(\kappa\Delta)}{\Delta^3}, \tag{C.11}$$

$$\kappa_4'^4 = -2\frac{4\cos(\kappa\Delta)-\cos(2\kappa\Delta)-3}{\Delta^4}, \tag{C.12}$$

$$\kappa_5'^5 = \frac{\sin(3\kappa\Delta)-4\sin(2\kappa\Delta)+5\sin(\kappa\Delta)}{\Delta^5}, \tag{C.13}$$

$$\kappa_6'^6 = 2\frac{-\cos(3\kappa\Delta)-15\cos(\kappa\Delta)+6\cos(2\kappa\Delta)+10}{\Delta^6}, \tag{C.14}$$

$$\kappa_7'^7 = -\frac{\sin(4\kappa\Delta)+14\sin(2\kappa\Delta)-14\sin(\kappa\Delta)-6\sin(3\kappa\Delta)}{\Delta^7}, \tag{C.15}$$

$$\kappa_8'^8 = -2\frac{-28\cos(2\kappa\Delta)+8\cos(3\kappa\Delta)+56\cos(\kappa\Delta)-\cos(4\kappa\Delta)-35}{\Delta^8}. \tag{C.16}$$

Appendix D. Germano's dynamic procedure for Burgers' equation

Here, we briefly revisit the dynamic procedure [31] applied to Burgers' equation. This dynamic procedure, allows to determine the model coefficient by comparing the resolved stress and the closure term on two different filter resolutions $\kappa_c = 2\pi/3\Delta$ and $\kappa_{c,2} = 2\pi/3\alpha\Delta$, where $\alpha = 2$ is typically chosen. With $\hat{\cdot}$ denoting the coarse filter, the multilevel formulation of the closure terms is then

$$\widetilde{u\tilde{u}} = \widetilde{\tilde{u}\tilde{u}} - 2C^2\Delta^2\left\langle\left|\frac{\delta\widetilde{\tilde{u}}}{\delta x}\right|\right\rangle_w\frac{\delta\tilde{u}}{\delta x}, \tag{D.1}$$

$$\widehat{u\hat{u}} = \widehat{\hat{u}\hat{u}} - 2C^2(\alpha\Delta)^2\left\langle\left|\frac{\delta\widehat{\hat{u}}}{\delta x}\right|\right\rangle_w\frac{\delta\hat{u}}{\delta x}. \tag{D.2}$$

Remark that we use the projective property of the sharp spectral filter $\widehat{\cdot} = \widehat{\widehat{\cdot}}$. The model coefficient C^2 can be extracted by comparing both equations on the same coarse resolution level, minimizing the error between both, leading to a least squares approximation for C^2

$$C^2 = \frac{\langle\mathcal{L}\mathcal{M}\rangle}{\langle\mathcal{M}\mathcal{M}\rangle}, \tag{D.3}$$

where

$$\mathcal{L} = \widehat{\tilde{u}\tilde{u}} - \widehat{\hat{u}\hat{u}}, \tag{D.4}$$

$$\mathcal{M} = 2\Delta_f^2\left[\left\langle\left|\frac{\delta\widetilde{\tilde{u}}}{\delta x}\right|\right\rangle_w\frac{\delta\tilde{u}}{\delta x} - \alpha^2\left\langle\left|\frac{\delta\widehat{\hat{u}}}{\delta x}\right|\right\rangle_w\frac{\delta\hat{u}}{\delta x}\right]. \tag{D.5}$$

References

[1] S. Ghosal, An analysis of numerical errors in large-eddy simulations of turbulence, J. Comput. Phys. 125 (1996) 187–206.
[2] A.G. Kravchenko, P. Moin, On the effect of numerical errors in large-eddy simulations of turbulent flows, J. Comput. Phys. 131 (1997) 310–322.
[3] F.K. Chow, P. Moin, A further study of numerical errors in large-eddy simulations, J. Comput. Phys. 184 (2003) 366–380.
[4] S.A. Orszag, On the elimination of aliasing in finite-difference schemes by filtering high-wavenumber components, J. Atmos. Sci. 28 (1971) 1074.
[5] N. Park, K. Mahesh, Analysis of numerical errors in large eddy simulation using statistical closure theory, J. Comput. Phys. 222 (2007) 194–216.
[6] J. Berland, C. Bogey, C. Bailly, A study of differentiation errors in large-eddy simulations based on the EDQNM theory, J. Comput. Phys. 227 (2008) 8314–8340.

[7] C.K.W. Tam, J.C. Webb, Dispersion-relation-preserving finite difference schemes for computational acoustics, J. Comput. Phys. 107 (1993) 262–281.
[8] J.W. Kim, D.T. Lee, Optimized compact finite difference schemes with maximum resolution, AIAA J. 34 (5) (1996) 887–893.
[9] R. Hixon, Nonlinear comparison of high-order and optimized finite-difference schemes, Int. J. Comput. Fluid Dynam. 13 (3) (2000) 259–277.
[10] G. Ashcroft, X. Zhang, Optimized prefactored compact schemes, J. Comput. Phys. 190 (2003) 459–477.
[11] C. Bogey, C. Bailly, A family of low dispersive and low dissipative explicit schemes for flow and noise computations, J. Comput. Phys. 194 (2004) 194214.
[12] G. Winckelmans, L. Georges, L. Bricteux, H. Jeanmart, The sampling-based dynamic procedure for LES in physical space, Bulletin of the American Physical Society Division of Fluid Dynamics 49 (9), 57th Annual Meeting of the American Physical Society Division of Fluid Dynamics, Seattle, Nov. 2004.
[13] G. Winckelmans, L. Bricteux, L. Georges, G. Daeninck, H. Jeanmart, The sampling-based dynamic procedure for LES: investigations using finite differences, in: E. Lamballais, R. Friederich, B. Geurts, O. Métais (Eds.), Ercoftac Series – Direct and Large-Eddy Simulations 6, Ercoftac, Springer, Poitiers, 2005, pp. 183–190.
[14] O. Debliquy, B. Knaepen, D. Carati, A.A. Wray, Sampling versus filtering in Large-Eddy simulations, in: P. Moin, N.N. Mansour (Eds.), Proceedings of the Summer Program 2004, Stanford University and Nasa AMES Research Center, Stanford, 2004, pp. 133–144.
[15] B. Knaepen, O. Debliquy, D. Carati, Large-eddy simulation without filter, J. Comput. Phys. 205 (2005) 98–107.
[16] D. Fauconnier, C. De Langhe, E. Dick, The dynamic procedure for accuracy improvement of numerical discretizations in fluid mechanics, J. Comput. Phys. 224 (2007) 1095–1123.
[17] D. Fauconnier, C. De Langhe, E. Dick, The sampling-based dynamic procedure as tool for higher-order discretization, Int. J. Numer. Methods Fluids 56 (2008) 1241–1247.
[18] J. Berland, C. Bogey, O. Marsden, C. Bailly, High-order, low dispersive and low dissipative explicit schemes for multiple-scale and boundary problems, J. Comput. Phys. 224 (2007) 637662.
[19] B. Vreman, B. Geurts, H. Kuerten, Comparison of numerical schemes in large-eddy simulations of the temporal mixing layer, Int. J. Numer. Methods Fluids 22 (1996) 297.
[20] J. Meyers, B. Geurts, M. Baelmans, Database analysis of errors in large-eddy simulation, Phys. Fluids 15 (9) (2003) 2740–2755.
[21] S.K. Lele, Compact finite difference schemes with spectral-like resolution, J. Comput. Phys. 103 (1991) 16–42.
[22] S. Pope, Turbulent Flows, Cambridge University Press, Cambridge, 2000.
[23] M.D. Love, Subgrid modelling studies with burgers'equation, J. Fluid Mech. 100 (1) (1980) 87–110.
[24] A. Das, R.D. Moser, Optimal large-eddy simulation of forced Burgers equation, Phys. Fluids 14 (12) (2002) 4344–4351.
[25] J.M. Burgers, Application of a model system to illustrate some points of the statistical theory of free turbulence, in: Nederl. Akad. Wetensch. Proc., vol. 43, 1940, pp. 2–12.
[26] G. De Stefano, O. Vasilyev, Sharp cutoff versus smooth filtering in large eddy simulation, Phys. Fluids 14 (1) (2002) 362–369.
[27] A. Domaradzki, D. Carati, An analysis of the energy transfer and the locality of nonlinear interactions in turbulence, Phys. Fluids 19 (8).
[28] A. Domaradzki, D. Carati, A comparison of spectral sharp and smooth filters in the analysis of nonlinear interactions and energy transfer in turbulence, Phys. Fluids 19 (8).
[29] T.S. Lund, On the Use of Discrete Filters for Large Eddy Simulation, Annual Research Briefs, Center for Turbulence Research, Stanford, 1997.
[30] D.C. Leslie, G.L. Quarini, The application of turbulence theory to the formulation of subgrid modelling procedures, J. Fluid Mech. 91 (1) (1979) 65–91.
[31] M. Germano, U. Piomelli, P. Moin, W.H. Cabot, A dynamic subgrid-scale eddy viscosity, Phys. Fluids A 3 (7) (1991) 1760–1765.
[32] J. Meyers, B. Geurts, P. Sagaut, A computational error-assessment of central finite-volume discretizations in large-eddy simulation using a Smagorinsky model, J. Comput. Phys. 227 (2007) 156–173.
[33] J. Meyers, B. Geurts, M. Baelmans, Optimality of the dynamic procedure for large-eddy simulations, Phys. Fluids 17 (4) (2005) 045–108.